Separate-phase model and its lattice Boltzmann algorithm for liquid-vapor two-phase flows in porous media

Shurong Lei and Yong Shi*

Department of Mechanical, Materials and Manufacturing Engineering, University of Nottingham Ningbo China, Ningbo 315100, China

(Received 29 April 2018; published 2 May 2019)

In this article, we formulate a set of the separate-phase governing equations at the representative-elementary-volume scale and develop its double-distribution function lattice Boltzmann (LB) algorithm to describe liquid-vapor two-phase flows with or without phase change in porous media. Different from those previous studies, the mathematical description in this article involves the Darcy force, viscous force, and pressure gradient, and the resulting LB simulations can well describe two-phase flows and mass transfer throughout porous media under the compounding effects of these forces. The LB algorithm was validated by simulating single-phase flows in porous media. Its results are in good agreement with those available analytical solutions. We also applied it to model water flows through a semi-infinite porous region bounded by a heated solid wall, where liquid-vapor phase change takes place. The numerical simulations recover the previous results in the limit of the zero Darcy number. Significantly, it reveals much richer two-phase flow and mass transfer characteristics in porous media adjacent to solid walls. The separate-phase model and its lattice Boltzmann algorithm in this article are effective means to gain more profound and clearer understandings of complex two-phase transport processes in a porous system.

DOI: 10.1103/PhysRevE.99.053302

I. INTRODUCTION

Porous media containing liquid and vapor are widely encountered in natural processes and modern industrial applications, such as subsurface contaminants [1,2], water movement in soils [3,4], building materials [5], heat transfer devices [6,7], food drying [8,9], fuel cells [10,11], etc. Flows of liquid and vapor in these multiphase systems are interdependent; meanwhile both are affected significantly by the existence of porous solid skeletons. These basic features differ much from the flows in void areas, leading liquid-vapor two-phase flows in porous media to possessing a number of unique flow characteristics.

Describing liquid-vapor two-phase flows in porous media relies on at what scale these transport phenomena are analyzed. A natural choice is the pore scale [12,13], at which flows of liquid and vapor are subject to the classical Navier-Stokes equations, together with appropriate liquid-vapor interfacial conditions and boundary conditions on the surfaces of solid grains (usually no slip if both fluid phases are continuum). From the theoretical point, the pore-scale models are well defined and are able to elaborate every flow detail; however, they require the full geometrical and structural information of porous skeletons which is usually practically unavailable [14]. Even though such information of every solid grain could be specified, solving these pore-scale models for a common porous system in engineering applications would be formidable, as they necessitate tremendous computational costs. To circumvent this issue, a paradigm shift was proposed in the early studies on flows in porous media. A larger scale, the representative-elementary-volume (REV) scale [15–18], was introduced, at which only the averaged multiphase flow characteristics of practical interest are captured with the aid of a set of effective transport properties determined from experiments. The simplest and most widely used REV-scale model is the Darcy equation [19] for single-phase flows, which links a nominal superficial velocity to the pressure heads imposed on the fluid phase at the two ends of porous media. This basic equation was later modified with consideration of the inertial force at high fluxes [20] and viscous effects in the vicinity of solid walls [21–24]. These modifications gave rise to the so-called Darcy-Forchheimer equation [25], Darcy-Brinkman equation [26], and even the Darcy-Forchheimer-Brinkman equation [27,28]. In comparison to the aforementioned pore-scale description, the REV-scale models do not require figuring out the exact geometries of the underlying porous networks, and thus their solving procedures are relatively simpler and more efficient. We point out, however, that the mathematical convenience at the REV scale is at the cost of loss of the pore-scale transport details. Accuracy of the REV-scale models heavily depends on the chosen effective transport properties. In the literature, a good and feasible REV-scale model must involve a set of effective properties which are well defined and can be fully specified from either experiments or other theoretical or numerical means.

Despite some deficiencies in the REV-scale description, it is still the mainstream methodology in today's studies on liquid-vapor two-phase flows in porous media. For this type of flow, the corresponding REV-scale models in the literature fall into two primary categories: separate-phase models [29,30] and mixture models [31–33]. The former describes liquid and

*Author to whom correspondence should be addressed: yong.shi@nottingham.edu.cn

vapor flows in porous media separately using different sets of REV-scale governing equations. It can thus resolve transport of each fluid phase. As to the mixture models, they treat liquid, vapor, and solid grains in every REV as a mixture with the effective mixture properties. A single set of governing equations is then proposed to capture flow characteristics of such a bulk mixture as a whole. Moreover, the mixture models usually include the governing equation of volume or mass fraction of one phase of interest so that they can describe mass transfer effectively pertinent to their applications. Among the various mixture models, the one developed by Wang and Beckermann [34,35] is a representative example. Such a model consists of three partial differential equations (PDEs) to solve the mixture pressure, velocity, and liquid saturation. Its advantage is that the model solves fewer PDEs in comparison with its separate-phase counterpart. The mixture model developed in Refs. [34,35] is formulated only based on Darcy's law nonetheless. This limits its application scope for real engineering applications, especially for the cases where porous media are confined by solid boundaries [36]. Here we point out that in the REV-scale framework the so-called Brinkman term is used to characterize the viscous effects [27]. However, inclusion of this term in a mixture model will lead the model to solving the same number of PDEs as the separate-phase models. Therefore, an introduction of the "mixture" concept does not bring any mathematical convenience in this scenario. Worse, its results are also less straightforward than those from the separate-phase models to manifest liquid and vapor flow and mass transfer characteristics explicitly. In this article, we hereby choose the separate-phase model as the REV-scale description for liquid-vapor two-phase flows in porous media with inclusion of the viscous effects.

A separate-phase model usually consists of several coupling PDEs, which need to be solved numerically except for a very few simple flow problems. The lattice Boltzmann (LB) method is an established numerical approach with more than three decade rapid development since it emerged [37–40]. The method, in particular those on-lattice LB models [41–44], has simple mathematics, favorable algorithmic structure, and easy programming. For many flow, heat and mass transfer problems, the LB method manifests itself with high accuracy, competitive efficiency, and good stability [45,46]. It is also deemed as one of the most promising numerical approaches and attracts tremendous interest in simulating fluid flows in porous media [47–49]. Again, the existing LB models for flows in porous media are classified as the pore-scale models [50–52] and REV-scale models [53,54]. For the pore-scale simulations, the previous studies primarily took advantage of the LB strength in dealing with complex-shaped boundaries [55,56]. Later, however, some studies discovered that the single-relaxation-time collision with the bounce-back rule was inaccurate—the LB results, after an upscaling average, led to a viscosity-dependent permeability [57–59]. To circumvent this issue, the so-called two-relaxation-time LB model [57,60], together with a large variety of sophisticated boundary treatments on solid-fluid interfaces [61,62], was proposed. In addition, application of the LB method to the pore-scale two-phase flows has also been spurred over recent years. In various versions these models primarily focus on the flows with bubbles or droplets in extremely small porous networks; see Refs. [63,64]. As to the REV-scale LB models, the majority of them were constructed through modifying the original LB evolution equations, equilibrium distributions, and quadrature rules so that they can effectively capture distinct transport characteristics in porous media. One representative is the so-called gray-scale LB models [65–67], which realize that each REV-scale point (i.e., a lattice node in the LB framework) includes both the solid and fluid phases. They make up fictitious underlying particle dynamics: $1 - n_s$ distribution functions on a lattice node are assumed to move subject to the original Boltzmann Bhatnagar-Gross-Krook (BGK) rule, whereas the rest of the n_s distribution functions experience the bounce-back reflection. Nonetheless, the applicability of such gray-scale LB models for two-phase flows is challenging, especially when the flows involve the nonlinear capillary force or Forchheimer inertial effects. In these scenarios, the partial bounce-back particle dynamics in the gray-scale LB models need to be justified in consideration of multiple coexisting fluids or phases, each experiencing more than the Darcy force. Instead of speculating virtual REV-scale particle dynamics, other studies proposed the LB models using some *ad hoc* source terms to describe porous-medium effects. The source terms are usually devised as polynomials in terms of the particle velocity [68], and the coefficients are specified given that the resulting model can recover the REV-scale governing equations exactly. So far, this kind of LB models well simulated single-phase flows at the REV scale [53,54], whereas an extension to liquid-vapor two-phase flows in porous media has not been well reported in the literature. The difficulties to be overcome include how to define the REV-scale fluid variables appropriately in the LB framework and design a workable coupling among different fluid phases.

The objective of this article is to study liquid-vapor two-phase flows in porous media at the REV scale. Different from the previous studies, we formulate a separate-phase model with the Brinkman term considering viscous effects in both the bulk porous region and vicinity of solid boundaries. Importantly, a double-distribution LB algorithm based on this separate-phase model is constructed in the simple on-lattice form. Through a series of simulations, we assess its numerical performance for the nonlinear liquid-vapor two-phase flows in porous media, and reveal the rich REV-scale multiphase flow and mass transfer characteristics.

The rest of this article is organized as follows: In Sec. II, we present a REV-scale separate-phase model and its dimensionless form for the liquid-vapor two-phase flows with phase change in porous media. We then develop a double-distribution function LB algorithm in Sec. III. In Sec. IV, we apply the LB algorithm to simulate the single-phase flows through a porous channel and liquid-vapor two-phase flows in semi-infinite porous media bounded by a heated bottom wall. In each case, we examine the numerical performance of the algorithm, and elaborate the corresponding transport characteristics based on the numerical results. Finally, we draw our conclusions in Sec. V and relegate the upscaling average, Chapman-Enskog expansion, dimensional analysis, and stability analysis to Appendixes A–D, respectively.

II. SEPARATE-PHASE MODEL FOR LIQUID-VAPOR TWO-PHASE FLOWS IN POROUS MEDIA AT THE REV SCALE

We focus on liquid-vapor two-phase flows with or without phase change in homogenous and isotropic porous media. In this article, we limit our discussion to steady and isothermal conditions. Through an upscaling average over the Stokes equations at the pore scale (see the details in Appendix A), we obtain a set of separate-phase governing equations at the REV scale. For the liquid phase, its governing equations are

$$\frac{\partial}{\partial \mathbf{X}} \cdot \mathbf{U}_l = \frac{M}{\rho_l}, \tag{1}$$

$$\frac{\varepsilon s \mu_l}{K_l}\mathbf{U}_l = -\varepsilon s \frac{\partial P_l^l}{\partial \mathbf{X}} + \mu_l \frac{\partial^2 \mathbf{U}_l}{\partial \mathbf{X}^2}, \tag{2}$$

while the vapor flow is subject to

$$\frac{\partial}{\partial \mathbf{X}} \cdot \mathbf{U}_v = -\frac{M}{\rho_v}, \tag{3}$$

$$\frac{\varepsilon(1-s)\mu_v}{K_v}\mathbf{U}_v = -\varepsilon(1-s)\frac{\partial P_v^v}{\partial \mathbf{X}} + \mu_v \frac{\partial^2 \mathbf{U}_v}{\partial \mathbf{X}^2}, \tag{4}$$

where the subscripts l and v represent liquid and its vapor, respectively. $\mathbf{X}$ is the REV-scale spatial coordinates. ε and s are the porous-medium porosity and liquid saturation. In Eqs. (1)–(4), $\{\rho_l, \mu_l, \mathbf{U}_l \text{ and } \mathrm{P}_l^l\}$ and $\{\rho_v, \mu_v, \mathbf{U}_v \text{ and } \mathrm{P}_v^v\}$ are the REV-scale density, viscosity, superficial-averaged velocity, intrinsic-averaged pressure of the liquid and vapor phases, respectively. M denotes the mass transfer between liquid and vapor due to phase change in a REV. Moreover, since the porous media are isotropic, the effective permeability $K_j (j = l, v)$ is expressed by

$$K_j = K k_{rj}, \quad j = l, v. \tag{5}$$

K and k_{rj} are the absolute and relative permeabilities. For water and steam, k_{rj} is a function of s [34], i.e.,

$$k_{rl} = s^n, \quad k_{rv} = (1-s)^n, \tag{6}$$

with $n = 3$. Moreover, the liquid intrinsic-averaged pressure links to its vapor counterpart by

$$P_c = P_v^v - P_l^l. \tag{7}$$

P_c is the capillary pressure specified by [6]

$$P_c = \sqrt{\frac{\varepsilon}{K}}\sigma J(S) = \sqrt{\frac{\varepsilon}{K}}\sigma[1.417(1-S) - 2.120(1-S)^2 + 1.263(1-S)^3], \tag{8}$$

with the liquid-vapor surface tension σ and

$$S = \frac{s - s'}{1 - s'}. \tag{9}$$

In Eq. (9), the residual liquid saturation s' represents an amount of liquid which is not removed by any means but evaporation. It is worth mentioning that the separate-phase model, i.e., Eqs. (1)–(4), is formulated in the Darcy-Brinkman form for both the liquid and vapor phases as we are interested in liquid-vapor two-phase flows at low speeds with the REV-scale viscous effects.

To better reflect the key flow characteristics in this complex multiphase system, we further derive the dimensionless form of Eqs. (1)–(9). We define the following dimensionless variables,

$$\mathbf{X}^* = \frac{\mathbf{X}}{L}, \quad \begin{pmatrix}\mathbf{U}_l^* \\ \mathbf{U}_v^*\end{pmatrix} = \frac{1}{U_0}\begin{pmatrix}\mathbf{U}_l \\ \mathbf{U}_v\end{pmatrix}, \quad \begin{pmatrix}P_l^{l*} \\ P_v^{v*}\end{pmatrix} = \frac{K}{\mu_l U_0 L}\begin{pmatrix}P_l^l - P_0 \\ P_v^v - P_0\end{pmatrix},$$
$$M^* = \frac{ML}{\rho_l U_0}, \quad \mathrm{Da} = \frac{K}{L^2}, \quad \mathrm{Ca} = \frac{\mu_l U_0}{\sigma}, \quad \mu^* = \frac{\mu_v}{\mu_l}, \quad \rho^* = \frac{\rho_v}{\rho_l}, \tag{10}$$

where L is the characteristic length and U_0 is the characteristic velocity. P_0, Da, and Ca are the reference pressure, Darcy number, and capillary number, respectively. With the aid of Eq. (10), the dimensionless separate-phase governing equations are

$$\frac{\partial}{\partial \mathbf{X}^*} \cdot \mathbf{U}_l^* = M^*, \tag{11}$$

$$\mathbf{U}_l^* = -\frac{\varepsilon s}{\alpha}\frac{\partial P_l^{l*}}{\partial \mathbf{X}^*} + \frac{\mathrm{Da}}{\alpha}\frac{\partial^2 \mathbf{U}_l^*}{\partial \mathbf{X}^{*2}}, \tag{12}$$

$$\frac{\partial}{\partial \mathbf{X}^*} \cdot (\rho^* \mathbf{U}_v^*) = -M^*, \tag{13}$$

$$\mathbf{U}_v^* = -\frac{\varepsilon(1-s)}{\beta \rho^* \mu^*}\frac{\partial\left(\rho^* P_v^{v*}\right)}{\partial \mathbf{X}^*} + \frac{\mathrm{Da}}{\beta \rho^*}\frac{\partial^2(\rho^* \mathbf{U}_v^*)}{\partial \mathbf{X}^{*2}}, \tag{14}$$

where the coefficients

$$\alpha = \frac{\varepsilon s}{k_{rl}}, \quad \beta = \frac{\varepsilon(1-s)}{k_{rv}}, \tag{15}$$

and

$$P_v^{v*} = P_l^{l*} + \frac{\sqrt{\mathrm{Da} \cdot \varepsilon}}{\mathrm{Ca}} J(S). \tag{16}$$

Equations (11)–(16) comprise a dimensionless REV-scale separate-phase model for liquid-vapor two-phase flows in porous media. In Sec. III, we will formulate a LB algorithm to solve these PDEs numerically.

III. LATTICE BOLTZMANN ALGORITHM

In this section, we propose a double-distribution function LB algorithm based on the separate-phase model to simulate liquid-vapor two-phase flows in porous media. For simplicity without loss of generality, our discussion is limited to two-dimensional (2D) problems. The proposed LB algorithm is also applicable to three-dimensional (3D) cases when the 2D discrete velocity space (i.e., D2Q9 [69]) is replaced by

its three-dimensional (3D) counterpart (e.g., D3Q15 [70]) in addition with proper boundary conditions specified in the new dimension.

We introduce two distribution functions, f_i, g_i, and their equilibria, f_i^{eq}, g_i^{eq}, for the liquid and vapor phases, respectively, in the discrete velocity space. To formulate the LB equations consistent with the dimensionless governing equations (11)–(14), we nondimensionalize these functions, together with other variables,

$$f_i^* = \frac{U_0 K}{L\mu_l} f_i, \quad f_i^{eq*} = \frac{U_0 K}{L\mu_l} f_i^{eq}, \quad g_i^* = \frac{U_0 K}{L\mu_l} g_i, \quad g_i^{eq*} = \frac{U_0 K}{L\mu_l} g_i^{eq},$$
$$t^* = \frac{t}{L/U_0}, \quad \Delta t^* = \frac{\Delta t}{L/U_0}, \quad \mathbf{c}_i^* = \frac{\mathbf{c}_i}{U_0}. \tag{17}$$

Here t^* and Δt^* denote the dimensionless time and time step, which are obtained by scaling their dimensional counterparts by the characteristic flow time L/U_0. $\mathbf{c}_i^*$ is the dimensionless discrete velocity with a speed $c^* = \Delta X^*/\Delta t^*$ (ΔX^* is the corresponding dimensionless lattice spacing at the REV scale). In this article, this discrete particle velocity $\mathbf{c}_i^*$ is specified using the D2Q9 scheme [69]. With these dimensionless variables given by Eq. (17), the LB evolution equations are

$$f_i^*(t^* + \Delta t^*, \mathbf{X}^* + \mathbf{c}_i^* \Delta t^*) - f_i^*(t^*, \mathbf{X}^*) = -\frac{1}{\tau_f}\left[f_i^*(t^*, \mathbf{X}^*) - f_i^{eq*}(t^*, \mathbf{X}^*)\right] + \Delta t^* F_i^*, \tag{18}$$

$$g_i^*(t^* + \Delta t^*, \mathbf{X}^* + \mathbf{c}_i^* \Delta t^*) - g_i^*(t^*, \mathbf{X}^*) = -\frac{1}{\tau_g}\left[g_i^*(t^*, \mathbf{X}^*) - g_i^{eq*}(t^*, \mathbf{X}^*)\right] + \Delta t^* G_i^*, \tag{19}$$

where τ_f and τ_g are the liquid and vapor dimensionless relaxation times, respectively. On the right-hand side of Eqs. (18) and (19), the equilibria, f_i^{eq*} and g_i^{eq*}, are expressed as polynomials in terms of $\mathbf{c}_i^*$. It follows that

$$f_i^{eq*} = w_i\left[\frac{\varepsilon s P_l^{l*}}{(c_s^*)^2} + \mathrm{Da}\frac{\mathbf{U}_l^* \cdot \mathbf{c}_i^*}{(c_s^*)^2}\right], \quad i = 0 - 8, \tag{20}$$

$$g_i^{eq*} = \begin{cases} (w_i - 1)\rho^* \frac{\varepsilon(1-s)P_v^{v*}}{(c_s^*)^2} + s, & i = 0 \\ w_i \rho^* \left[\frac{\varepsilon(1-s)P_v^{v*}}{(c_s^*)^2} + \mathrm{Da}\frac{\mathbf{U}_v^* \cdot \mathbf{c}_i^*}{(c_s^*)^2}\right], & i = 1 - 8 \end{cases}, \tag{21}$$

where the sound speed $c_s^* = c^*/\sqrt{3}$ and w_i is the moment weight pertinent to $\mathbf{c}_i^*$ [69]. Importantly, two source terms, F_i^* and G_i^* in Eqs. (18) and (19), are introduced,

$$F_i^* = \begin{cases} \left(w_i - \frac{1}{2}\right)\left(2 - \frac{1}{\tau_f}\right)\mathrm{Da}M^*, & i = 0 \\ w_i\left(2 - \frac{1}{\tau_f}\right)\left[\mathrm{Da}M^* + \frac{\mathbf{F}^* \cdot \mathbf{c}_i^*}{2(c_s^*)^2}\right], & i = 1 - 8 \end{cases}, \tag{22}$$

and

$$G_i^* = \begin{cases} \left(w_i - \frac{1}{2}\right)\left(\frac{1}{\tau_g} - 2\right)\mathrm{Da}M^*, & i = 0 \\ w_i\left(\frac{1}{\tau_g} - 2\right)\left[\mathrm{Da}M^* - \frac{\mathbf{G}^* \cdot \mathbf{c}_i^*}{2(c_s^*)^2}\right], & i = 1 - 8 \end{cases}, \tag{23}$$

where

$$\mathbf{F}^* = -\alpha \mathbf{U}_l^* + P_l^{l*}\frac{\partial(\varepsilon s)}{\partial \mathbf{X}^*}, \quad \mathbf{G}^* = -\beta \rho^* \mu^* \mathbf{U}_v^* + \rho^* P_v^{v*}\frac{\partial[\varepsilon(1-s)]}{\partial \mathbf{X}^*}. \tag{24}$$

We constructed these two source terms following the idea proposed by Guo *et al.* [68]. However, Eqs. (22)–(24) are formulated to recover the Darcy-Brinkman equation, whereas the external-force treatments in Ref. [68] are for Navier-Stokes equations. The latter are the governing equations for continuum flows at the pore scale. It is also worth noting that Eq. (24) includes the spatial derivatives of s and ε. In this work, we assume the porosity ε is constant and apply the second-order central-difference scheme to discretize these gradients, i.e.,

$$\left.\frac{\partial(\varepsilon s)}{\partial X^*}\right|_{X_i^*, Y_i^*} \approx \frac{\varepsilon}{2\Delta X^*}[s(X_i^* + \Delta X^*, Y_i^*) - s(X_i^* - \Delta X^*, Y_i^*)]. \tag{25}$$

Here we take the derivative with respect to X^* as an example for demonstration. With f_i^* and g_i^*, the liquid and vapor variables are now computed by

$$\frac{\varepsilon s P_l^{l*}}{(c_s^*)^2} = \sum_i f_i^* + \frac{\Delta t^*}{2}\mathrm{Da}M^*, \quad \mathbf{U}_l^* = \left(\sum_i f_i^* \mathbf{c}_i^* + \frac{\Delta t^*}{2}\mathbf{F}^*\right)\Big/ \mathrm{Da}, \tag{26}$$

$$s = \sum_i g_i^* - \frac{\Delta t^*}{2}\mathrm{Da}M^*, \qquad \rho^* \mathbf{U}_v^* = \left(\sum_i g_i^* \mathbf{c}_i^* + \frac{\Delta t^*}{2}\mathbf{G}^*\right)\Big/ \mathrm{Da}. \tag{27}$$

We point out that through the Chapman-Enskog expansion, Eqs. (18), (20), (22), and (26) recover the liquid-phase governing equations (11) and (12), whereas Eqs. (13) and (14) for the vapor phase are derived from Eqs. (19), (21), (23), and (27). The two relaxation times $\tau_f = 1/[(c_s^*)^2\Delta t^*] + 0.5$ and $\tau_g = \mu^*/[(c_s^*)^2\Delta t^*] + 0.5$ (interested readers can refer to Appendix B for the detailed Chapman-Enskog expansion). Meanwhile, note that the LB algorithm, Eqs. (18)–(27), is a time-dependent numerical solver for the steady-state governing equations (11)–(14). This may raise doubts about its effectiveness when modeling the steady-state two-phase flows in porous media. To be clear, we point out the governing equations (11)–(14) are a nonlinear system for the unknowns $\mathbf{U}_l^*$, P_l^{l*}, $\mathbf{U}_v^*$, and s. From the computational point of view, these partial differential equations are solved numerically in an iterative manner. No direct solver is available. On the other hand, time in the current LB framework is not a genuine contributing variable as only the steady-state solutions are of interest to us. The LB evolution procedure with "time" acts essentially as iterative steps towards the convergence (steady state) of the nonlinear equations (11)–(14). Significantly, in comparison to other conventional iterative solvers, this LB algorithm possesses simple mathematics and on-lattice numerics. These lead to quite a few favorable numerical strengths, such as easy programming, second-order accuracy, CFL (the Courant-Friedrichs-Lewy number) = 1.0, and so on. In implementation, the iteration of the LB algorithm consists of nine steps:

(1) Initialize the REV-scale fields $\mathbf{U}_l^{*,(0)}$, $\mathbf{U}_v^{*,(0)}$, $P_l^{l*,(0)}$, and $s^{(0)}$, and specify the effective properties and dimensionless numbers ε, ρ^*, μ^*, Da, Ca, and M^*.

(2) Compute the equilibrium distribution $f_i^{eq*,(k)}$ and source term $F_i^{*,(k)}$, where $k = 1, 2, \cdots$, for the liquid phase using Eqs. (20) and (22), respectively.

(3) Update the distribution functions $f_i^{*,(k)}$ throughout the computational domain using the evolution equation (18) with the given boundary conditions.

(4) With $f_i^{*,(k)}$, compute its moments to obtain the liquid pressure $P_l^{l*,(k)}$ and velocity $\mathbf{U}_l^{*,(k)}$ by Eq. (26).

(5) Update the vapor pressure $P_v^{v*,(k)}$ by $P_l^{l*,(k)}$ and $s^{(k-1)}$ using Eq. (16).

(6) Compute $g_i^{eq*,(k)}$ using Eq. (21) and $G_i^{*,(k)}$ using Eq. (23) based on $s^{(k-1)}$, $\mathbf{U}_v^{*,(k-1)}$, and $P_v^{v*,(k)}$.

(7) Apply the evolution equation (19) to update the distribution functions $g_i^{*,(k)}$.

(8) Use Eq. (27) to update $s^{(k)}$ and $\mathbf{U}_v^{*,(k)}$ as the moments of $g_i^{*,(k)}$.

(9) Repeat steps 2–8 until the LB simulation reaches its convergence.

In summary, a LB algorithm based on the REV-scale separate-phase model is developed in this section. This algorithm consists of Eqs. (18)–(27) and its computational procedure includes nine steps. We will apply it to study liquid-vapor two-phase flows in porous media numerically in Sec. IV.

IV. NUMERICAL RESULTS AND DISCUSSION

In this section, we will apply the LB algorithm developed in Sec. III to simulate liquid-vapor two-phase flows in porous media. As a numerical study, we will first validate the accuracy of our LB algorithm by simulating a single-phase flow problem through a porous channel bounded by two solid walls. Comparison to the available analytical solutions is conducted. We will then extend our numerical discussion to liquid-vapor two-phase flows through porous media bounded by a heated bottom solid plate, at which phase change between liquid and vapor takes place. Importantly, we will explore in detail the compounding effects of phase distribution and the viscous boundary layer in this multiphase flow system.

A. Single-phase flows through a porous channel

We first apply the LB algorithm in Sec. III to simulate the single-phase flows through a two-dimensional square porous channel bounded by two solid walls; see Fig. 1. In this problem, a fluid is driven by a pressure difference, $P_{\mathrm{in}} - P_{\mathrm{out}}(P_{\mathrm{in}} > P_{\mathrm{out}})$, imposed at the channel's two ends. The channel's height and length are L and it is filled with

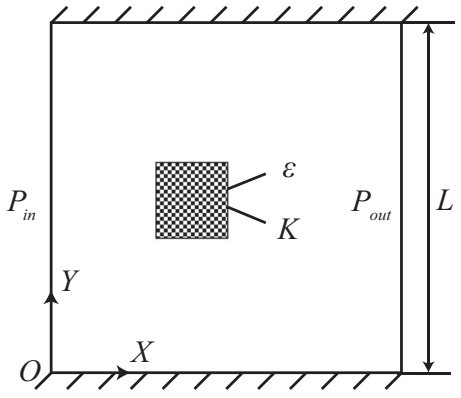

FIG. 1. Schematic of the single-phase flows through a square porous channel. The origin of the coordinates is at the bottom-left corner of the channel.

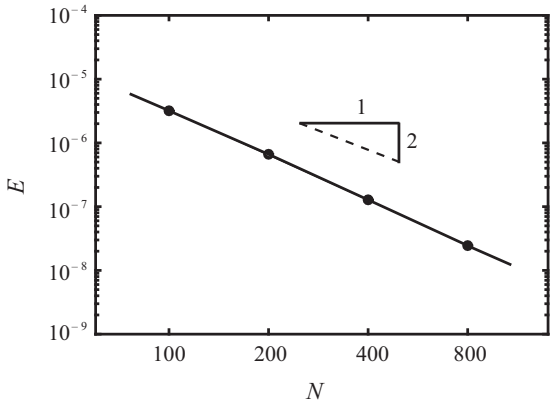

FIG. 2. The L_1-norm of errors obtained on the 100×100, 200×200, 400×400, and 800×800 grids for the single-phase flows through a square porous channel.

homogenous and isentropic porous media with the porosity ε and permeability K. The top and bottom walls are solid and impermeable, on which the no-slip boundary conditions for the REV-scale fluid velocities are employed.

For this problem, the fluid velocity at the REV scale is solved analytically,

$$U^* = 1 - \frac{\cosh(2\theta Y^* - \theta)}{\cosh(\theta)}, \quad V^* = 0, \tag{28}$$

where $\theta = 1/(2\sqrt{\mathrm{Da}/\varepsilon})$, $(X^*, Y^*) = (X, Y)/L$, and $(U^*, V^*) = (U, V)/U_0$. U^* and V^* are the dimensionless velocity components in the X^* and Y^* directions and the characteristic velocity $U_0 = K(P_{\mathrm{in}} - P_{\mathrm{out}})/(\mu L)$.

We set the saturation $s = 1$ and conducted the LB simulation only for the distribution function f_i^* and its moments in this single-phase flow problem. In simulation, we chose $\tau_f = 1.0029$ and the Mach number $\mathrm{Ma} = 2.87 \times 10^{-3}$ to ensure the incompressible condition was well met. As to the boundary conditions, we used P_{out} as the reference, which led to the dimensionless inlet and outlet pressures $P_{\mathrm{in}}^* = 1$ and $P_{\mathrm{out}}^* = 0$. These pressure conditions were implemented to assign f_i^* at the inlet and outlet in our codes using the non-equilibrium scheme [71]. Such a scheme was also applied to specify f_i^* on the top and bottom walls subject to the no-slip boundary conditions.

Grid-independence tests were examined on 100×100, 200×200, 400×400, and 800×800 grids. Importantly, to quantify numerical accuracy, the L_1-norm of errors was introduced,

$$E = \sqrt{\frac{1}{N^2}\sum_i (U_i^* - \tilde{U}_i^*)^2}, \tag{29}$$

where U_i^* is the streamwise velocity obtained from the LB simulation and $\tilde{U}_i^*$ is its analytical solution. i denotes the ith grid (lattice) node and N is the total node number in the computational domain. For demonstration, we took the flow at $\mathrm{Da} = 5 \times 10^{-4}$ and $\varepsilon = 0.5$ as an example. Figure 2 shows the resulting L_1-norm of errors given by the LB simulations on the four grids. It is clear that the LB algorithm is second-order accurate, and its global error on 100×100 grids has dropped to the order of magnitude of 10^{-6}. For the single-phase flows under investigation, we thus deem the results on 100×100 grids to be accurate enough in comparison to the analytical solutions.

Through use of the 100×100 grids, we then performed a series of LB simulations for the flows with the Darcy numbers ranging from $\mathrm{Da} = 5 \times 10^{-5}$ to 5×10^{-3}, but a constant porosity $\varepsilon = 0.5$. Figure 3 shows the obtained dimensionless streamwise velocities U^*. It is seen that the velocity profiles display variations with the changing Darcy numbers. To be specific, the profile of U^* exhibits a pronounced decay from its bulk value $U_b^* = 1$ at the channel center to $U_w^* = 0$ on the two solid walls when the Darcy number is large; see line C in Fig. 3(a). On the other hand, when the Darcy number becomes small, such a velocity exhibits an almost unchanged profile in the majority of the bulk region, whereas it drops steeply in a very narrow vicinity of the walls. Interestingly, we also investigated the impacts of the porosity on the flow. Figure 3(b) shows different streamwise velocities when the porosity ranges from $\varepsilon = 0.3$ to 0.7 at $\mathrm{Da} = 5 \times 10^{-4}$. Different from those in Fig. 3(a), the distributions of U^* in Fig. 3(b) are less sensitive to the changing porosity—its profiles in the given three cases almost collapse into a single line; they differ slightly from one another at a small region when U^* drops from U_b^*.

Theoretically, the aforementioned dual impacts of the Darcy number and porosity on flow in porous media can be integrated by introducing a combined dimensionless group Da/ε. Figure 4 summarizes the results in Fig. 3 through use of Da/ε. Importantly, Fig. 4 also shows the analytical solutions given by Eq. (28) for comparison. We see in Fig. 4 that although the magnitudes of Da/ε jump across several orders, all the velocities obtained from the LB simulations are well agreed with the corresponding analytical solutions. This confirms the second-order accuracy of the LB algorithm shown in Fig. 2 for simulating the single-phase flows in porous media. Crucially, the results in Fig. 4 exhibit that the streamwise velocities U^* in all cases experience a continuous decay from its bulk value U_b^* to the wall boundary condition U_w^*. This is understandable because we employed the no-slip boundary conditions on the walls and the LB algorithm includes the Brinkman term. The latter characterizes the REV-scale viscous effects throughout the entire porous zone.

We point out that the flow features in Fig. 4 resemble the velocity distributions in the classical boundary layer in the void flow region. Inspired by this analog, we defined a REV-scale "boundary layer" in this article and introduced a dimensionless length, $\delta^* = \delta/L$, the ratio of its thickness δ to the channel width L. This dimensionless thickness is computed as a distance in the Y^* direction from the wall to a locus where $U^*|_{Y^*=\delta^*} = 0.99U_b^*$. Based on these definitions, Fig. 5 shows δ^* in the double logarithm coordinates when the porosity changes from $\varepsilon = 0.3$ to 0.7 while the Darcy number changes from $\mathrm{Da} = 3 \times 10^{-5}$ to 7×10^{-4}. It shows that δ^* grows gradually with the increasing Darcy number while it achieves a large value when a porous medium has a small ε. We formulate a relation of δ^* to Da and ε based on the results in Fig. 5, i.e.,

$$\ln \delta^* \approx \frac{1}{2}\ln\frac{\mathrm{Da}}{\varepsilon} + 1.526. \tag{30}$$

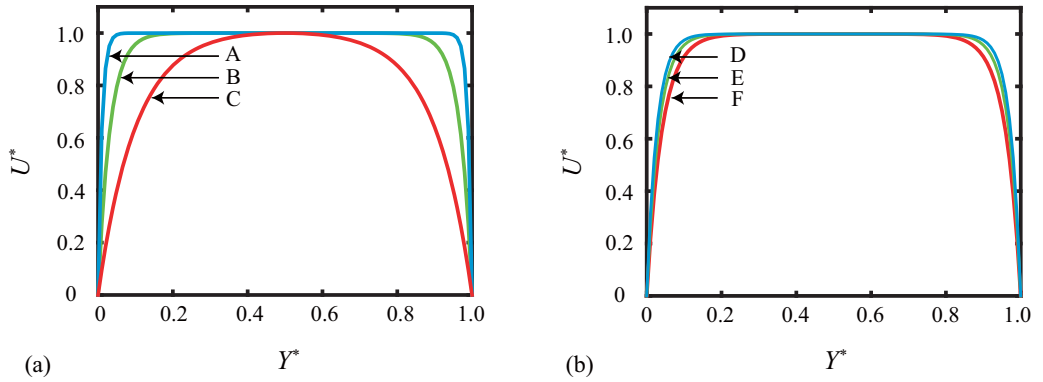

FIG. 3. The dimensionless streamwise velocity U^* in the single-phase flows through a square porous channel. (a) A: Da $= 5 \times 10^{-5}$, $\varepsilon = 0.5$; B: Da $= 5 \times 10^{-4}$, $\varepsilon = 0.5$; C: Da $= 5 \times 10^{-3}$, $\varepsilon = 0.5$. (b) D: Da $= 5 \times 10^{-4}$, $\varepsilon = 0.7$; E: Da $= 5 \times 10^{-4}$, $\varepsilon = 0.5$; F: Da $= 5 \times 10^{-4}$, $\varepsilon = 0.3$.

Actually, Da$/\varepsilon$ characterizes the magnitude of the viscous force in comparison to that of the Darcy force. A large Da$/\varepsilon$ indicates that the viscous force is dominating in the flow, and thus the boundary layer is rather thick. On the contrary, when Da$/\varepsilon$ is small, the Darcy force will surpass the viscous force. Under its influence, U^* will retain its bulk value in the majority of the channel cross section, whereas it only decays rapidly in a thin layer near the walls.

In summary, the numerical results in this subsection demonstrate that the LB algorithm in Sec. III can simulate the single-phase flows in porous media with high accuracy. Importantly, due to inclusion of the Brinkman term in its framework, the LB simulations reveal two distinct characteristic lengths—the channel height L and the REV-scale boundary-layer thickness δ. Their ratio δ^* is proportional to $\sqrt{\text{Da}/\varepsilon}$, which characterizes the importance of the viscous force against the Darcy force in the flows in porous media.

B. Liquid-vapor two-phase flows in porous media

Next, we extend the LB algorithm to porous media containing both the liquid and vapor phases. To be specific, we consider liquid water flows through a semi-infinite porous region bounded by a bottom solid plate; see Fig. 6. Such a flow is driven by an external pressure difference $(P_{\text{in}} - P_{\text{out}})$ in the X direction, and the porous media in use are homogenous and isotropic. Their porosity and permeability are denoted by ε and K. Furthermore, the bottom plate is heated so that liquid water in contact with it is evaporated into vapor. This results in the saturation on the bottom wall $s_w < 1$.

We simulated this problem within a square domain above the hot solid plate with a side length L. Critically, L in simulation was set large enough so that the bottom plate exerted negligible impacts on the flow in the upper areas far from the wall. The corresponding boundary conditions are given as follows,

$$P_l^{l*}\big|_{X^*=0,Y^*\geqslant 0} = 1, \quad s|_{X^*=0,Y^*\geqslant 0} = s_b, \tag{31a}$$

$$P_l^{l*}\big|_{X^*=1,Y^*\geqslant 0} = 0, \quad \left.\frac{\partial s}{\partial X^*}\right|_{X^*=1,Y^*\geqslant 0} = 0, \tag{31b}$$

$$U_l^*|_{X^*\geqslant 0,Y^*=0} = 0, \quad V_l^*|_{X^*\geqslant 0,Y^*=0} = 0, \quad s|_{X^*\geqslant 0,Y^*=0} = s_w, \tag{31c}$$

$$\left.\frac{\partial U_l^*}{\partial Y^*}\right|_{X^*\geqslant 0,Y^*=1} = 0, \quad \left.\frac{\partial V_l^*}{\partial Y^*}\right|_{X^*\geqslant 0,Y^*=1} = 0, \quad s|_{X^*\geqslant 0,Y^*=1} = s_b, \tag{31d}$$

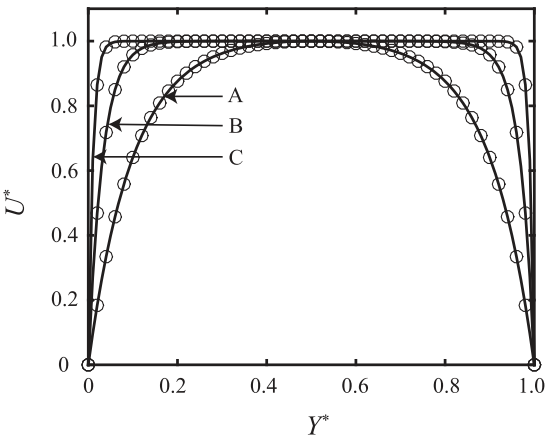

FIG. 4. The dimensionless streamwise velocity U^* in the single-phase flows through a square porous channel. Solid lines: analytical solutions to Eq. (28); open circles: the LB results. A: Da$/\varepsilon = 10^{-2}$; B: Da$/\varepsilon = 10^{-3}$; C: Da$/\varepsilon = 10^{-4}$.

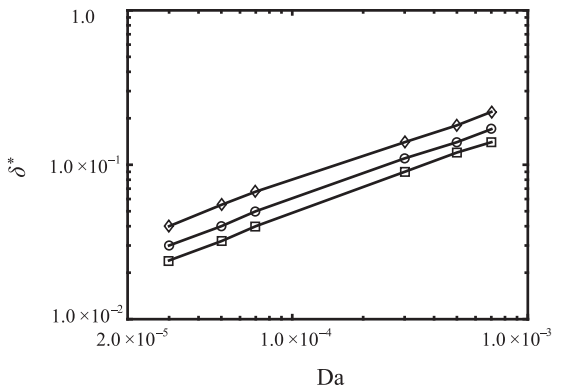

FIG. 5. The dependence of δ^* on different ε and Da. Diamonds: $\varepsilon = 0.3$; circles: $\varepsilon = 0.5$; squares: $\varepsilon = 0.7$.

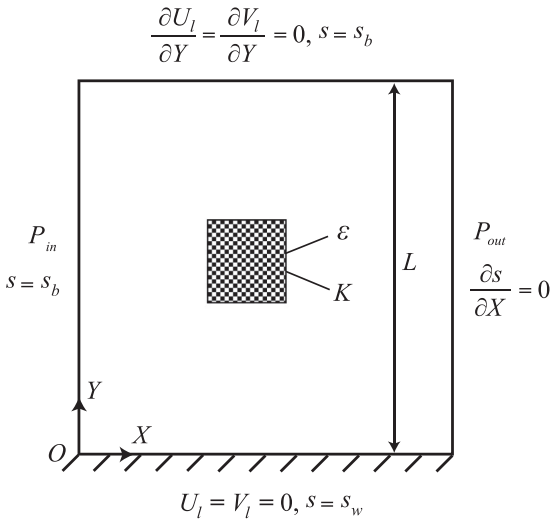

FIG. 6. Schematic of the liquid-vapor two-phase flows through a semi-infinite porous region. The origin of the coordinates is at the bottom-left corner.

where $(X^*, Y^*) = (X, Y)/L$, $P_l^{l*} = (P_l^l - P_{\text{out}})/(P_{\text{in}} - P_{\text{out}})$, and $(U_l^*, V_l^*) = (U_l, V_l)/U_0$. Again, the characteristic velocity $U_0 = K(P_{\text{in}} - P_{\text{out}})/(\mu L)$. In Eqs. (31c) and (31d), s_w and s_b are the saturations on the bottom plate and in the bulk region far from the bottom plate. In simulation, we specified $s_w = 0.8$ and $s_b = 1$. The Dirichlet boundary conditions were realized in the LB code using the non-equilibrium scheme [71], while it was also applied to specify the Neumann boundary conditions [54]. Moreover, we set the density ratio $\rho^* = 6.23 \times 10^{-4}$, viscosity ratio $\mu^* = 4.25 \times 10^{-2}$, and capillary number $\text{Ca} = 0.1$ by referring to the properties of water and its vapor at the standard atmospheric pressure. The residual liquid saturation s' was specified as zero following the treatment in Ref. [35]. In addition, we chose the two dimensionless relaxation times as $\tau_f = 1.0029$, $\tau_g = 0.5214$ and the Mach number $\text{Ma} = 1.44 \times 10^{-3}$. The latter can guarantee a good approximation of the incompressible condition. In this article, we did not consider the buoyancy and gravity.

Again, the LB simulations were conducted on 100×100, 200×200, 400×400, and 800×800 grids for grid-independence tests. For demonstration, we chose the streamwise mixture momentum (defined as $\rho_0^* U^* = U_l^* + \rho^* U_v^*$ with $\rho_0^* = s + (1 - s)\rho^*$ [35]) at $X^* = 0.5$ with $\text{Da} = 1 \times 10^{-3}$ and $\varepsilon = 0.5$ as an example. Figure 7 shows its profiles from the LB simulations on the four grids. It is seen that the results on the 200×200, 400×400, and 800×800 grids collapse nearly into a single line while only those on 100×100 grids deviate slightly. This indicates that the 200×200 grids are sufficiently good for the LB simulation of this two-phase flow problem.

Furthermore, we computed the L_1-norm of errors from the numerical results based on the four grids. Since no analytical solutions are available for this two-phase problem, we used the results on the 800×800 grids as the benchmarks and plotted the L_1-norms of the other three coarse grids in Fig. 8. Again, the LB algorithm exhibits the second-order numerical accuracy for this liquid-vapor two-phase problem studied in this section.

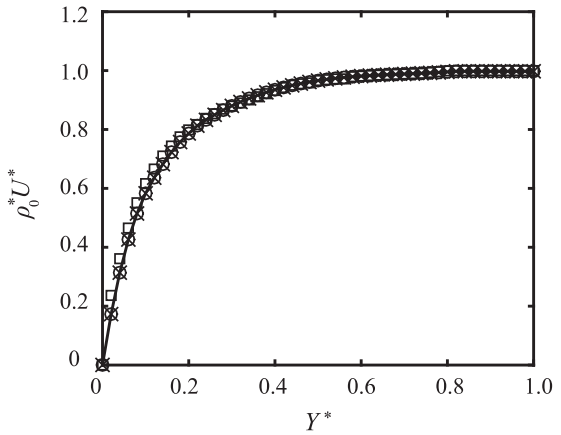

FIG. 7. The streamwise mixture momenta $\rho_0^* U^*$ at $X^* = 0.5$ with $\text{Da} = 1 \times 10^{-3}$ and $\varepsilon = 0.5$. Squares: 100×100; open circles: 200×200; crosses: 400×400; solid line: 800×800.

In addition to numerical accuracy, we also assessed the stability of the LB algorithm for this two-phase flow problem. We conducted the von Neumann linearized stability analysis and Appendix D summarizes the relevant mathematical formulas. We found that the evolution of perturbations of the two distribution functions in the wave-number space depends on the three coefficient matrices $\tilde{\mathbf{A}}$, $\tilde{\mathbf{B}}$, and $\tilde{\mathbf{C}}$; see Eqs. (D9) and (D10). The stability of this LB algorithm necessitates the maximum eigenvalue modulus of each matrix equal to or smaller than unity [72,73]. For the case with the wave number $\mathbf{k} = 0$, the stability boundaries of the LB algorithm are $\tau_f > 1/2$ and $\tau_g > 1/2$. However, these boundaries become difficult to clarify for the two-phase flows when $\mathbf{k} \neq 0$. We find that in such general flows, the eigenvalues of $\tilde{\mathbf{A}}$ and $\tilde{\mathbf{B}}$ rely on $\mathbf{k}$, ε, Da, τ_f, and ΔX^* while the latter also rely on the dimensionless reference streaming velocity U^0. As to the matrix $\tilde{\mathbf{C}}$, its eigenvalues are the functions of $\mathbf{k}$, τ_g, ΔX^*, and $\rho^* \varepsilon P^0/(c_s^*)^2$. Here P^0 is the dimensionless pressure at the reference background. For the liquid-vapor two-phase problem studied in this section, we set the porosity $\varepsilon = 0.5$ and the grid spacing $\Delta X^* = 0.005$ (i.e., 200 grids). Moreover, we chose $U^0 = 1$, $P^0 = 1$ and limited our analyses to the most probable unstable condition, where the wave

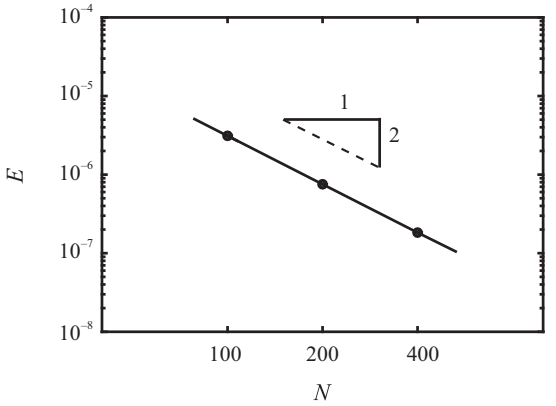

FIG. 8. The L_1-norm of errors obtained on the 100×100, 200×200, and 400×400 grids for the liquid-vapor two-phase flows through a semi-infinite porous region.

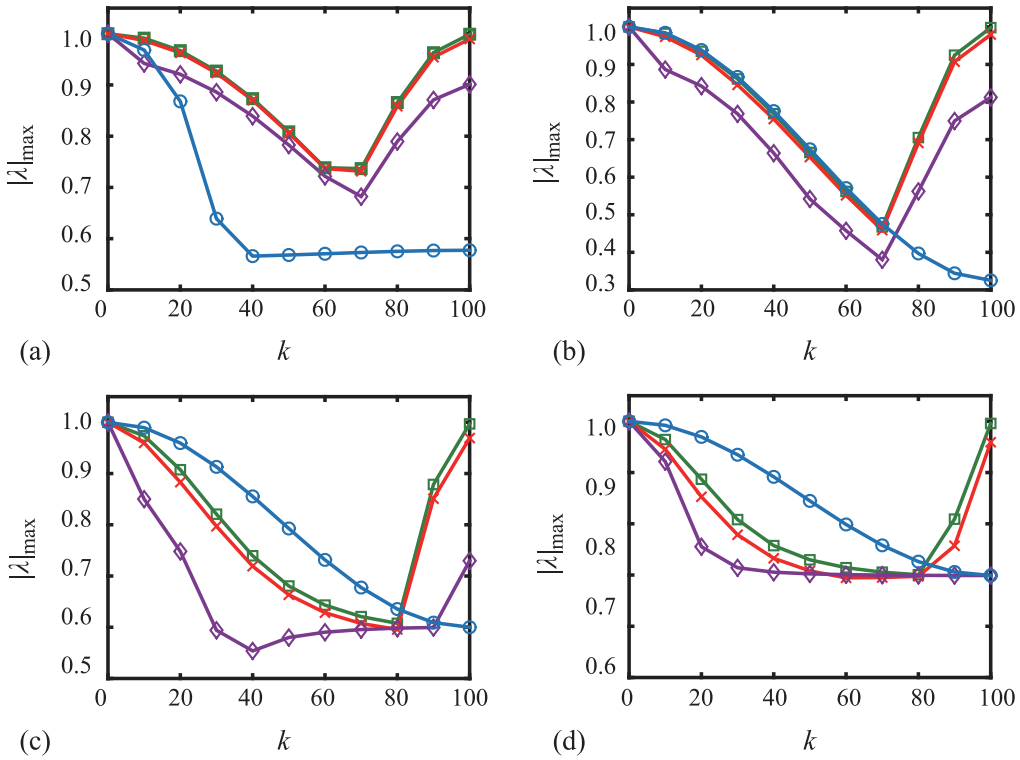

FIG. 9. Dependence of $|\lambda|_{\max}$ of the matrix $\tilde{\mathbf{A}}$ on the wave number k. (a) $\tau_f = 0.75$; (b) $\tau_f = 1.0$; (c) $\tau_f = 1.25$; (d) $\tau_f = 1.5$. Circles: $\mathrm{Da} = 10^{-6}$; diamonds: $\mathrm{Da} = 10^{-5}$; crosses: $\mathrm{Da} = 10^{-4}$; squares: $\mathrm{Da} = 10^{-3}$.

number is parallel to the reference streaming velocity [43] (for convenience, we denote the wave number in the streaming direction by k in the following). We computed numerically the maximum eigenvalue moduli, $|\lambda|_{\max}$, of the three coefficient matrices with different wave numbers, relaxation times, and Darcy numbers. Figures 9 and 10 show the resulting $|\lambda|_{\max}$ of $\tilde{\mathbf{A}}$ and $\tilde{\mathbf{B}}$, respectively, when $\tau_f = 0.75$, 1, 1.25, 1.5 and $\mathrm{Da} = 10^{-6}$, 10^{-5}, 10^{-4}, 10^{-3}. It is worth mentioning that

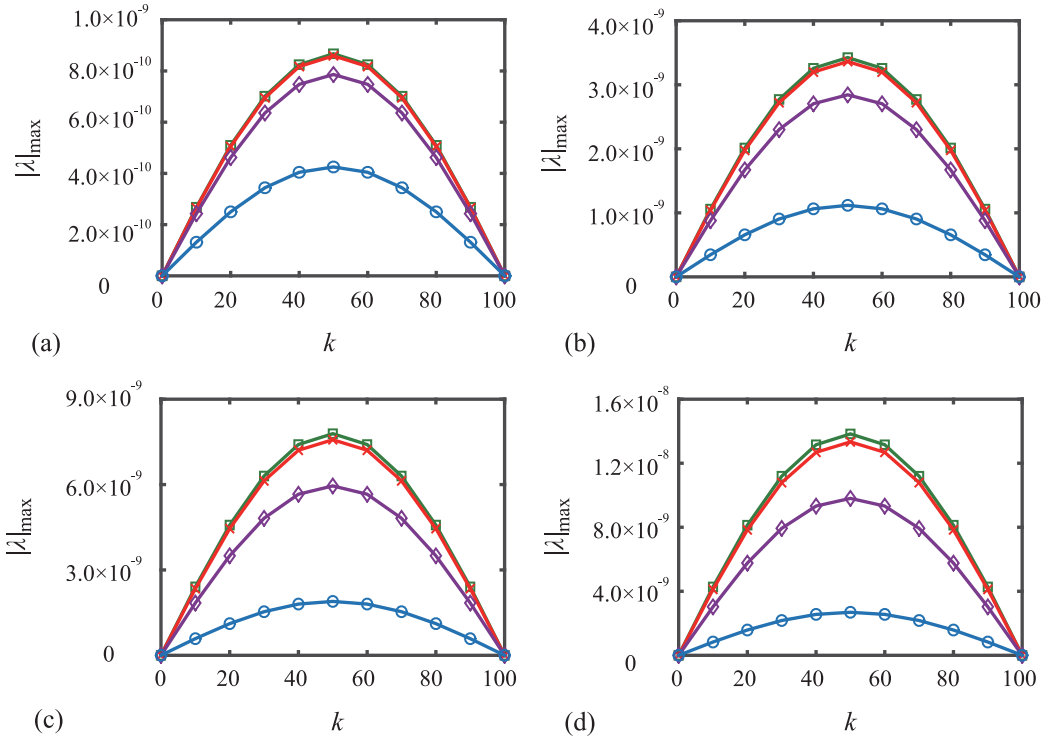

FIG. 10. Dependence of $|\lambda|_{\max}$ of the matrix $\tilde{\mathbf{B}}$ on the wave number k. (a) $\tau_f = 0.75$; (b) $\tau_f = 1.0$; (c) $\tau_f = 1.25$; (d) $\tau_f = 1.5$. Circles: $\mathrm{Da} = 10^{-6}$; diamonds: $\mathrm{Da} = 10^{-5}$; crosses: $\mathrm{Da} = 10^{-4}$; squares: $\mathrm{Da} = 10^{-3}$.

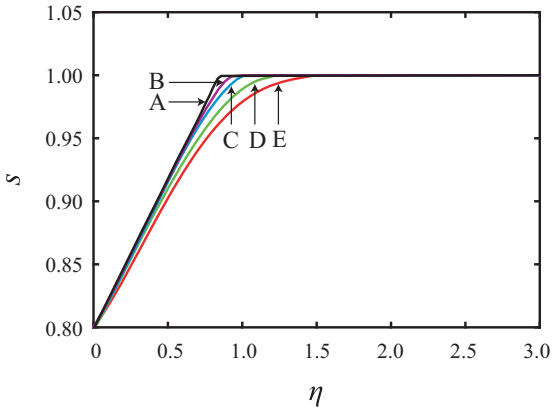

FIG. 11. The saturation s with different Darcy numbers. A: Results from Ref. [35]; B: Da $= 10^{-6}$; C: Da $= 10^{-5}$; D: Da $= 10^{-4}$; E: Da $= 10^{-3}$.

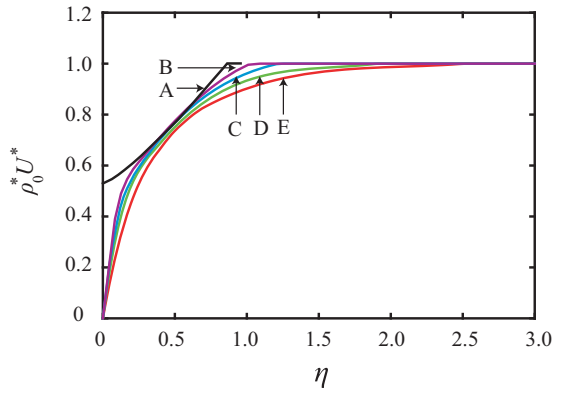

FIG. 12. The profiles of $\rho_0^* U^*$ with different Darcy numbers. A: Results from Ref. [35]; B: Da $= 10^{-6}$; C: Da $= 10^{-5}$; D: Da $= 10^{-4}$; E: Da $= 10^{-3}$.

since the maximum eigenvalue moduli are axisymmetric with respect to $k_N = 100N$ $(N = 1, 2, 3, \cdots)$, both figures only show the results in the range of $0 \leqslant k \leqslant 100$. We see that all the maximum eigenvalue moduli of the coefficient matrices $\tilde{\mathbf{A}}$ and $\tilde{\mathbf{B}}$ are not larger than unity under the current numerical settings. This indicates the distribution function f_i^* in the LB simulation evolves stably in the wave-number space with different τ_f and Da. We also computed the maximum eigenvalue modulus of $\tilde{\mathbf{C}}$, whose values are equal to unity irrespective of the varying k, τ_g, and Da. We confirm that the distribution function g_i^* is also stable in simulation. However, it should be noted that these stability results should be rejustified when the reference U^0 and P^0 are specified in different values. This is mainly because the maximum eigenvalue modulus of $\tilde{\mathbf{B}}$ depends on U^0 while that of $\tilde{\mathbf{C}}$ depends on P^0. Nonetheless, the $|\lambda|_{\max}$ of $\tilde{\mathbf{B}}$ would be beyond unity only if U^0 were on the order of 10^8 under the current numerical settings. Moreover, if we were to choose any pressure in the computational domain as P^0, the $|\lambda|_{\max}$ of $\tilde{\mathbf{C}}$ would never exceed 1.

To conclude, the stability of the LB algorithm proposed in this article depends on multiple factors including porous-medium properties (ε and Da), numerical setting (ΔX^*, τ_f, and τ_g), flow conditions ($\mathbf{U}^0$, P^0), and liquid and vapor properties (μ^* and ρ^*). Our current numerical settings well guarantee accuracy and stability of the LB algorithm for the liquid-vapor two-phase flow problem shown in Fig. 6. In the following, we will conduct the LB simulation to reveal the multiphase mass transfer and flow characteristics in porous media.

We focus on the two-phase flows with the Darcy numbers changing from Da $= 1 \times 10^{-6}$ to Da $= 1 \times 10^{-3}$. Considering that the flows in porous media are less sensitive to the changing porosity as shown in Sec. IV A, we set the porosity $\varepsilon = 0.5$. Figure 11 shows the resulting saturations for the flows with Da $= 10^{-6}$, 10^{-5}, 10^{-4}, and 10^{-3}. Here to better exhibit the saturation profiles, we introduced a new coordinate $\eta = Y/\delta_s(X)$ [35]. δ_s is the thickness of a two-phase layer, in which the saturation $s_w < s(X) < s_b$. We clarify that this coordinate transform is necessary as the saturation s varies in both the X and Y directions; however, its profiles along the X direction could be affine in this problem. Through a dimensional analysis (see details in Appendix C), we obtained the two-phase layer thickness, $\delta_s(X) \sim O[(\varepsilon\mathrm{Da})^{1/4}\sqrt{XL/\mathrm{Ca}}]$, and

$$\eta = \left(\frac{\mathrm{Ca}^2}{\varepsilon\mathrm{Da}}\right)^{1/4} \frac{Y^*}{\sqrt{X^*}}. \tag{32}$$

In Fig. 11, we see that the saturations in different Xs collapse into one single line when the Darcy number is given. This justified the similarity of s in the X direction. Furthermore, the saturation grows monotonically with the increasing η from s_w on the solid plate to s_b in the bulk porous region. This is consistent with the underlying fluid physics—vapor is generated by phase change on the bottom heated plate. It then mixes with the surrounding liquid water to form a two-phase layer. When moving further away from the plate, the vapor contents drop and finally disappear in the bulk flow region. Note that the saturation profiles in Fig. 11 vary with different Darcy numbers—a flow at a large Darcy number always exhibits a smoother saturation distribution, and its two-phase layer is thicker than that at a smaller Da. In addition, Fig. 11 also plots the results from Ref. [35] that solved a mixture model without inclusion of the Brinkman viscous term. We see an abrupt bend in its saturation profile at the onset of the drop from s_b. Its two-phase layer thickness is smaller than our results, whose Darcy numbers are finite.

We next turn our attention to the velocities in this multiphase system. To compare with the results in Ref. [35], we computed the mixture momentum, $\rho_0^*\mathbf{U}^*$, based on our numerical results. Figures 12 and 13 show its components in the X and Y directions (i.e., $\rho_0^* U^*$ and $\rho_0^* V^*$), respectively. Again, we employed η in these figures and rescaled $\rho_0^* V^*$ by $1/\xi$ [$\xi = \sqrt[4]{\mathrm{Ca}^2 X^{*2}/(\varepsilon\mathrm{Da})}$] so that its variation in the narrow vicinity of the solid plate can be clearly illustrated. As shown in Figs. 12 and 13, $\rho_0^* U^*$ and $\rho_0^* V^* \xi$ only depend on η for each flow at different Darcy numbers, implying that the mixture momentum is affine in the X direction. Meanwhile, the viscous boundary layers are identified in both figures, across which $\rho_0^* U^*$ and $\rho_0^* V^* \xi$ gradually decay from their bulk values to their boundary values on the bottom walls. In comparison to the results of the mixture model [35], we see the streamwise $\rho_0^* U^*$ obtained from our LB simulation does

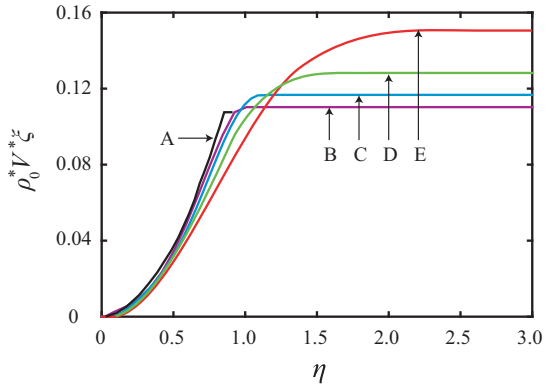

FIG. 13. The profiles of $\rho_0^* V^* \xi$ with different Darcy numbers. A: Result from Ref. [35]; B: Da $= 10^{-6}$; C: Da $= 10^{-5}$; D: Da $= 10^{-4}$; E: Da $= 10^{-3}$.

not slip on the wall and exhibits a much smoother profile in the viscous boundary layer. Moreover, its boundary-layer thickness grows with the increasing Darcy number; compare Lines B–E in Fig. 12. These transport details in the viscous boundary layer have not been revealed by the previous multiphase mixture model as it does not include the Brinkman term in its framework.

As to the cross-stream component $\rho_0^* V^* \xi$, Fig. 13 shows its profiles rely more heavily on the Darcy number. For example, in the flow with a large Darcy number, its profile varies more steeply and its bulk value is much bigger than that with a smaller Darcy number. We note that though the magnitude of the cross-stream component is rather small in comparison to its streamwise counterpart, it is a contributing factor to driving vapor from the solid walls into the bulk porous region.

It is worth recalling that the strength of the separate-phase model is that it can elaborate the transport details of both the liquid and vapor phases explicitly. Figures 14 and 15 show the streamwise and cross-stream components of the liquid velocity $\mathbf{U}_l^*$ and vapor velocity $\mathbf{U}_v^*$ from the LB simulations. Again, these functions are found self-affined in the streamwise direction—they are only dependent on η. Moreover, explicit viscous boundary layers are well observed in both figures to represent the viscous effects near the solid walls at the REV scale. We note, however, the thickness of the vapor viscous

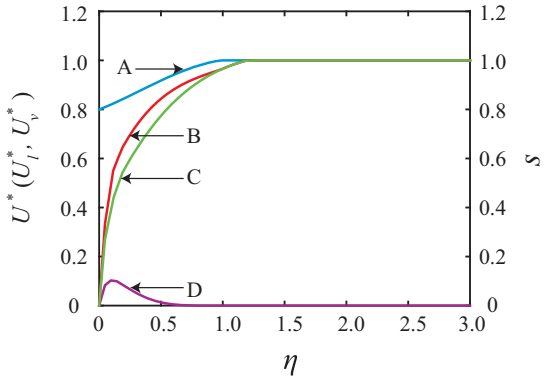

FIG. 14. The profiles of the streamwise velocities and saturation at Da $= 10^{-5}$. A: Saturation s; B: mixture U^*; C: liquid U_l^*; D: vapor U_v^*.

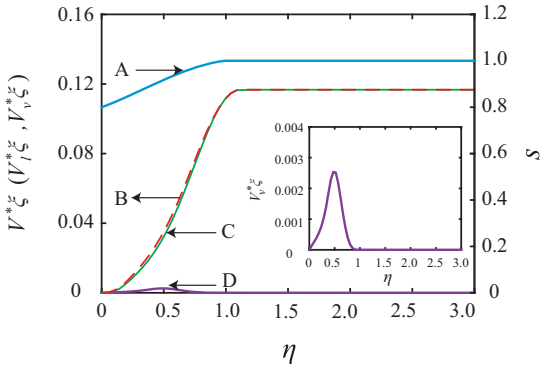

FIG. 15. The profiles of the cross-streamwise velocities and saturation at Da $= 10^{-5}$. A: Saturation s; B: mixture $V^*\xi$; C: liquid $V_l^*\xi$; D: vapor $V_v^*\xi$. Inset: the details of $V_v^*\xi$.

boundary layer is much smaller than that of the liquid viscous boundary layer. We explain this phenomenon with the aid of the dimensional analysis—the thicknesses of the liquid and vapor viscous boundary layers are $\delta_l \sim O(\sqrt{\mathrm{Da}/\varepsilon} L s_0)$ and $\delta_v \sim O[\sqrt{\mathrm{Da}/\varepsilon} L(1 - s_0)]$, respectively. Since the liquid phase in this problem is dominant, $s_0 > (1 - s_0)$, it is thus not surprising that we have $\delta_v < \delta_l$. In addition to $\mathbf{U}_l^*$ and $\mathbf{U}_l^*$, Figs. 14 and 15 further show the mixture velocity $\mathbf{U}^*$ for a direct comparison. It is plain that the profiles of $\mathbf{U}^*$ are very close to those of $\mathbf{U}_l^*$, but far different from those of $\mathbf{U}_v^*$. Therefore, we see that the previous mixture model is ineffective in describing the vapor flow in this problem.

It is interesting to compare the liquid and vapor viscous boundary layers with the two-phase layer. To this end, Figs. 14 and 15 also include the saturation profile. Here we take Fig. 14 as an example. We see the thickness of the two-phase layer δ_s is on an order comparable with that of the liquid viscous boundary layer δ_l, both of which are far larger than the thickness of the vapor viscous boundary layer δ_v. These results evidence that the liquid flow in the two-phase layer is viscous dominant, whereas the viscous effects in the vapor-phase flow are confined within a thin region at the bottom of the two-phase layer.

The numerical simulations shown in Figs. 11–15 demonstrate the separate-phase model can characterize much richer mass transfer and flow features than the previous mixture model for complex multiphase flow systems. The LB algorithm developed in this article is a useful numerical means to reveal this information and assist in analyzing the pertinent flow phenomena.

V. CONCLUSION

Liquid-vapor two-phase flows with or without phase change in porous media are a crucial and representative flow and mass transfer problem in a large variety of natural and engineering occasions. In this article, we present a set of separate-phase governing equations with inclusion of the viscous effects to describe these complex transport phenomena at the REV scale. Importantly, we developed a double-distribution LB algorithm based on this separate-phase model to simulate flows and mass transfer of liquid and its vapor effectively in both the bulk porous region and the vicinity of solid boundaries.

We assessed the LB algorithm by simulating the single-phase flows through a square porous channel and two-phase flows in semi-infinite porous media bounded by a bottom solid plate. The numerical results demonstrate the LB algorithm constructed in this work is an effective iterative solver for the nonlinear liquid-vapor flow problems in porous media. It is second-order accurate and stable with little impacts from the finite difference approximation of its source terms. Importantly, the simulations given by the LB model well capture nonlinear interactions between liquid and vapor phases at the REV scale, and elaborate clearly mass transfer of the two fluid phases within the two-phase layer and rich flow characteristics in the liquid and vapor viscous boundary layers. Our future work will advance along this avenue to apply the LB method to study three-dimensional liquid-vapor two-phase flows in porous media with thermal effects.

ACKNOWLEDGMENTS

The authors would like to acknowledge support from Zhejiang Provincial Natural Science Foundation of China under Grant No. LY16E060001, Ningbo Science and Technology Bureau Technology Innovation Team (Grant No. 2016B10010), and Ningbo International Cooperation Program (Grant No. 2015D10018). S.L. acknowledges financial support by China Scholarship Council (No. 201708330304).

APPENDIX A: UPSCALING AVERAGE FROM THE PORE SCALE TO REV SCALE FOR TWO-PHASE FLOWS WITH PHASE CHANGE IN POROUS MEDIA

In this Appendix, we apply the upscaling volume average to derive the REV-scale separate-phase model from the transport details at the pore scale. We start the demonstration by assuming that both liquid and vapor at the pore scale are incompressible and subject to the Stokes equation [15],

$$\frac{\partial}{\partial \mathbf{x}} \cdot \mathbf{u}_l = 0, \tag{A1}$$

$$0 = -\frac{\partial p_l}{\partial \mathbf{x}} + \mu_l \frac{\partial^2 \mathbf{u}_l}{\partial \mathbf{x}^2}, \tag{A2}$$

while

$$\frac{\partial}{\partial \mathbf{x}} \cdot \mathbf{u}_v = 0, \tag{A3}$$

$$0 = -\frac{\partial p_v}{\partial \mathbf{x}} + \mu_v \frac{\partial^2 \mathbf{u}_v}{\partial \mathbf{x}^2}. \tag{A4}$$

$\mathbf{x}$ denotes the pore-scale spatial coordinates, and the subscripts l and v represent the liquid and vapor phases, respectively. ρ_j, μ_j, $\mathbf{u}_j$, and p_j (where $j = l$ or v) are the density, viscosity, pore-scale velocity, and pressure of each fluid phase. At the liquid-solid-vapor interfaces, the corresponding interfacial conditions are employed,

$$\mathbf{u}_l|_{A_{ls}} = 0, \tag{A5}$$

$$\mathbf{u}_v|_{A_{vs}} = 0, \tag{A6}$$

$$\mathbf{u}_l|_{A_{lv}} = \mathbf{u}_v|_{A_{lv}}, \tag{A7}$$

and

$$-p_l|_{A_{lv}}\mathbf{n}_{lv} + \tau_l|_{A_{lv}} \cdot \mathbf{n}_{lv} = -p_v|_{A_{lv}}\mathbf{n}_{lv} + \tau_v|_{A_{lv}} \cdot \mathbf{n}_{lv} + 2(\sigma H)|_{A_{lv}}\mathbf{n}_{lv}, \tag{A8}$$

where A_{ij} represents the interfacial areas between phase i and phase j, and $\mathbf{n}_{ij}$ is the unit vector normal to this interface pointing from phase i to phase j. $p_k|_{A_{ij}}$ and $\tau_k|_{A_{ij}}$ are the interfacial pressure and shear stress of phase k on the interface A_{ij}, respectively. σ and H are the liquid-vapor surface tension and mean interface curvature.

To derive the REV-scale description, two kinds of upscaling averages are defined [74], i.e., the superficial average

$$\Phi_j = \frac{1}{V}\int_{V_j} \phi_j dV, \tag{A9}$$

and the intrinsic average

$$\Phi_j^j = \frac{1}{V_j}\int_{V_j} \phi_j dV, \tag{A10}$$

where V is the representative elementary volume and V_j is the volume occupied by phase j in V. ϕ_j is a pore-scale property of phase j. Importantly, a pore-scale spatial derivative of ϕ_j links to its REV counterpart by

$$\frac{1}{V}\int_{V_j} \frac{\partial \phi_j}{\partial \mathbf{x}} dV = \frac{\partial \Phi_j}{\partial \mathbf{X}} + \sum_{i \neq j} \frac{1}{V}\int_{A_{ji}} \mathbf{n}_{ji}\phi_j dA. \tag{A11}$$

A_{ji} is the interfacial (boundary) areas of phase j in V. Here we point out that to distinguish the spatial coordinates $\mathbf{x}$ at the pore scale, we use $\mathbf{X}$ to represent its counterpart at the REV scale.

With the aid of Eqs. (A5), (A6), and (A10), we integrate Eqs. (A1) and (A3) over a REV using the superficial average defined by Eq. (A9). The resulting REV-scale continuity equations for liquid and vapor are

$$\frac{\partial}{\partial \mathbf{X}} \cdot \mathbf{U}_l = \frac{M}{\rho_l}, \tag{A12}$$

and

$$\frac{\partial}{\partial \mathbf{X}} \cdot \mathbf{U}_v = -\frac{M}{\rho_v}, \tag{A13}$$

where M denotes the mass transfer between the liquid and vapor phase due to phase change in a REV. $\mathbf{U}_l$ and $\mathbf{U}_v$ are the REV-scale liquid and vapor seepage velocities, respectively.

In a similar manner, we apply the same upscaling average to derive the REV-scale liquid and vapor momentum transport equations from Eqs. (A2) and (A4). For demonstration, we take the liquid phase as an example, whose REV-scale momentum equation from Eq. (A2) is

$$0 = -\varepsilon s\frac{\partial P_l^l}{\partial \mathbf{X}} + \mu_l \frac{\partial^2 \mathbf{U}_l}{\partial \mathbf{X}^2} + \frac{1}{V}\int_{A_{ls}+A_{lv}} \mathbf{n}_l \cdot \left(\mu_l \frac{\partial \tilde{\mathbf{u}}_l}{\partial \mathbf{x}} - \tilde{p}_l \mathbf{I}\right) dA, \tag{A14}$$

where $\mathbf{I}$ is the second-rank unit tensor and $\mathbf{n}_l$ is the unit vector on the interfaces A_{ls} and A_{lv} pointing from the liquid

phase. In Eq. (A14), we introduced $\tilde{p}_l$ and $\tilde{\mathbf{u}}_l$, which represent the perturbations of the local pore-scale pressure and velocity to the corresponding REV-scale intrinsic averages, respectively. Note that we have dropped a term, $R = \mu_l \frac{\partial}{\partial \mathbf{X}} \cdot (\frac{1}{V}\int_{A_{l_v}} \mathbf{n}_{l_v}\mathbf{u}_l dA)$, from Eq. (A14) as the dimensional analysis confirms it is negligibly small when the pore-scale characteristics length is far smaller than the REV-scale characteristics length. Importantly, the interfacial integral on the right-hand side of Eq. (A14) corresponds to the Darcy force. It can be simplified by introducing the liquid permeability $\mathbf{K}_l$ [15] which leads to

$$\varepsilon s \mu_l (\mathbf{K}_l)^{-1} \cdot \mathbf{U}_l = -\varepsilon s \frac{\partial P_l^l}{\partial \mathbf{X}} + \mu_l \frac{\partial^2 \mathbf{U}_l}{\partial \mathbf{X}^2}. \tag{A15}$$

For the vapor phase, we follow the same averaging and derive its REV-scale momentum equation,

$$\varepsilon(1-s)\mu_v (\mathbf{K}_v)^{-1} \cdot \mathbf{U}_v = -\varepsilon(1-s)\frac{\partial P_v^v}{\partial \mathbf{X}} + \mu_v \frac{\partial^2 \mathbf{U}_v}{\partial \mathbf{X}^2}. \tag{A16}$$

Equations (A12) and (A15), (A13) and (A16), form the separate-phase model in this article for liquid-vapor two-phase flows in porous media at the REV scale. In contrast to the mixture model, this separate-phase model can elaborate mass and momentum transfer of liquid and vapor in porous media, respectively.

APPENDIX B: CHAPMAN-ENSKOG EXPANSION TO RECOVER THE REV-SCALE SEPARATE-PHASE GOVERNING EQUATIONS FROM THE LB ALGORITHM

We elaborate the Chapman-Enskog expansion in this Appendix, by which we recovered the dimensionless separate-phase governing equations (11)–(14) from the LB algorithm proposed in Sec. III. We first perform Chapman-Enskog multiscale expansion to the dimensionless distribution functions, temporal and spatial derivatives, and source terms, respectively:

$$f_i^* = f_i^{*(0)} + \mathrm{Kn} f_i^{*(1)} + \mathrm{Kn}^2 f_i^{*(2)} + \cdots, \tag{B1}$$

$$g_i^* = g_i^{*(0)} + \mathrm{Kn} g_i^{*(1)} + \mathrm{Kn}^2 g_i^{*(2)} + \cdots. \tag{B2}$$

$$\frac{\partial}{\partial t^*} = \mathrm{Kn}\frac{\partial_1}{\partial t^*} + \mathrm{Kn}^2 \frac{\partial_2}{\partial t^*}, \tag{B3}$$

$$\frac{\partial}{\partial \mathbf{X}^*} = \mathrm{Kn} \cdot \frac{\partial_1}{\partial \mathbf{X}^*}, \tag{B4}$$

$$M^* = \mathrm{Kn} M^{*(1)}, \quad \mathbf{F}^* = \mathrm{Kn} \cdot \mathbf{F}^{*(1)}, \quad \mathbf{G}^* = \mathrm{Kn} \cdot \mathbf{G}^{*(1)}. \tag{B5}$$

We then expand $f_i^*(t^* + \Delta t^*, \mathbf{X}^* + \mathbf{c}_i^* \Delta t^*)$ about $f_i^*(t^*, \mathbf{X}^*)$ and $g_i^*(t^* + \Delta t^*, \mathbf{X}^* + \mathbf{c}_i^* \Delta t^*)$ about $g_i^*(t^*, \mathbf{X}^*)$ using the Taylor series. Through combining these Taylor expansions with Eqs. (B1)–(B5), we rewrite Eqs. (18) and (19) as a series of equations in different order of the Knudsen number,

$$\mathrm{Kn}^0 : f_i^{*(0)} = f_i^{eq*}, \tag{B6}$$

$$\mathrm{Kn}^1 : \frac{d_1 f_i^{*(0)}}{dt^*} = -\frac{1}{\tau_f \Delta t^*} f_i^{*(1)} + F_i^{*(1)}, \tag{B7}$$

$$\mathrm{Kn}^2 : \frac{\partial_2 f_i^{*(0)}}{\partial t^*} + \left(1 - \frac{1}{2\tau_f}\right)\frac{d_1 f_i^{*(1)}}{dt^*} = -\frac{1}{\tau_f \Delta t^*} f_i^{*(2)} - \frac{\Delta t^*}{2}\frac{d_1 F_i^{*(1)}}{dt^*}, \tag{B8}$$

and

$$\mathrm{Kn}^0 : g_i^{*(0)} = g_i^{eq*}, \tag{B9}$$

$$\mathrm{Kn}^1 : \frac{d_1 g_i^{*(0)}}{\partial t^*} = -\frac{1}{\tau_g \Delta t^*} g_i^{*(1)} + G_i^{*(1)}, \tag{B10}$$

$$\mathrm{Kn}^2 : \frac{\partial_2 g_i^{*(0)}}{\partial t^*} + \left(1 - \frac{1}{2\tau_g}\right)\frac{d_1 g_i^{*(1)}}{dt^*} = -\frac{1}{\tau_g \Delta t^*} g_i^{*(2)} - \frac{\Delta t^*}{2}\frac{d_1 G_i^{*(1)}}{dt^*}, \tag{B11}$$

where the material derivative $d_1/dt^* = \partial_1/\partial t^* + \mathbf{c}_i^* \cdot \partial_1/\partial \mathbf{X}^*$. The quadratures of f_i^{eq*}, g_i^{eq*}, $F_i^{*(1)}$, and $G_i^{*(1)}$ in different orders are

$$\begin{aligned}
&\sum_i f_i^{eq*} = \varepsilon s P_l^{l*}/(c_s^*)^2, && \sum_i g_i^{eq*} = s,\\
&\sum_i f_i^{eq*}\mathbf{c}_i^* = \mathrm{Da}\mathbf{U}_l^*, && \sum_i g_i^{eq*}\mathbf{c}_i^* = \mathrm{Da}\rho^*\mathbf{U}_v^*,\\
&\sum_i f_i^{eq*}\mathbf{c}_i^*\mathbf{c}_i^* = \varepsilon s P_l^{l*}\mathbf{I}, && \sum_i g_i^{eq*}\mathbf{c}_i^*\mathbf{c}_i^* = \varepsilon(1-s)\rho^* P_v^{v*}\mathbf{I},
\end{aligned} \tag{B12}$$

$$\begin{aligned}
&\sum_i F_i^{*(1)} = \frac{2\tau_f - 1}{2\tau_f}\mathrm{Da}M^{*(1)}, && \sum_i G_i^{*(1)} = \frac{1-2\tau_g}{2\tau_g}\mathrm{Da}M^{*(1)},\\
&\sum_i F_i^{*(1)}\mathbf{c}_i^* = \frac{2\tau_f - 1}{2\tau_f}\mathbf{F}^{*(1)}, && \sum_i G_i^{*(1)}\mathbf{c}_i^* = \frac{1-2\tau_g}{2\tau_g}\mathbf{G}^{*(1)},\\
&\sum_i F_i^{*(1)}\mathbf{c}_i^*\mathbf{c}_i^* = \frac{2\tau_f - 1}{\tau_f}\mathrm{Da}M^{*(1)}(c_s^*)^2\mathbf{I}, && \sum_i G_i^{*(1)}\mathbf{c}_i^*\mathbf{c}_i^* = \frac{1-2\tau_g}{\tau_g}\mathrm{Da}M^{*(1)}(c_s^*)^2\mathbf{I}.
\end{aligned} \tag{B13}$$

Moreover, taking advantage of Eqs. (B6), (B9), (B12), (B13), (26), and (27), we further obtain

$$\sum_i f_i^{*(1)} = -\frac{\Delta t^*}{2}\mathrm{Da}M^{*(1)}, \qquad \sum_i f_i^{*(k)} = 0, \quad (k = 2, 3, \cdots),$$
$$\sum_i f_i^{*(1)}\mathbf{c}_i^* = -\frac{\Delta t^*}{2}\mathbf{F}^{*(1)}, \qquad \sum_i f_i^{*(k)}\mathbf{c}_i^* = 0, \quad (k = 2, 3, \cdots), \tag{B14}$$

$$\sum_i g_i^{*(1)} = \frac{\Delta t^*}{2}\mathrm{Da}M^{*(1)}, \qquad \sum_i g_i^{*(k)} = 0, \quad (k = 2, 3, \cdots),$$
$$\sum_i g_i^{*(1)}\mathbf{c}_i^* = -\frac{\Delta t^*}{2}\mathbf{G}^{*(1)}, \qquad \sum_i g_i^{*(k)}\mathbf{c}_i^* = 0, \quad (k = 2, 3, \cdots). \tag{B15}$$

Next, we multiply both sides of Eqs. (B7) and (B8) by 1 and sum over all discrete velocities. It follows that

$$\frac{\partial_1\left[\varepsilon s P_l^{l*}/(c_s^*)^2\right]}{\partial t^*} + \frac{\partial_1}{\partial \mathbf{X}^*}\cdot(\mathrm{Da}\mathbf{U}_l^*) = \mathrm{Da}M^{*(1)}, \tag{B16}$$

$$\frac{\partial_2\left[\varepsilon s P_l^{l*}/(c_s^*)^2\right]}{\partial t^*} = 0. \tag{B17}$$

The same manipulation is repeated but using a different multiplier $\mathbf{c}_i^*$. This results in two REV-scale momentum-like equations in the order of Kn and Kn^2,

$$\frac{\partial_1 \mathbf{U}_l^*}{\partial t^*} = -\frac{1}{\mathrm{Da}}\frac{\partial_1 \varepsilon s P_l^{l*}}{\partial \mathbf{X}^*} + \frac{\mathbf{F}^{*(1)}}{\mathrm{Da}}, \tag{B18}$$

$$\frac{\partial_2 \mathbf{U}_l^*}{\partial t^*} = \left(\tau_f - \frac{1}{2}\right)(c_s^*)^2\Delta t^* \times\left[\frac{\partial_1^2}{\partial \mathbf{X}^{*2}}\mathbf{U}_l^* + \frac{\partial_1}{\partial \mathbf{X}^*}\left(\frac{\partial_1}{\partial \mathbf{X}^*}\cdot\mathbf{U}_l^*\right) - \frac{\partial_1 M^{*(1)}}{\partial \mathbf{X}^*}\right]. \tag{B19}$$

Add Eq. (B16) to Eq. (B17) and Eq. (B18) to Eq. (B19). Under the steady states, the resulting equations are

$$\frac{\partial}{\partial \mathbf{X}^*}\cdot\mathbf{U}_l^* = M^*, \tag{B20}$$

$$\mathbf{U}_l^* = -\frac{\varepsilon s}{\alpha}\frac{\partial P_l^{l*}}{\partial \mathbf{X}^*} + \frac{\mathrm{Da}}{\alpha}\left(\tau_f - \frac{1}{2}\right)\Delta t^*(c_s^*)^2\frac{\partial^2 \mathbf{U}_l^*}{\partial \mathbf{X}^{*2}}, \tag{B21}$$

where $\tau_f = 1/[(c_s^*)^2\Delta t^*] + 0.5$. It is plain that Eqs. (B20) and (B21) are the governing equations for the liquid phase in porous media at the REV scale.

In a similar manner, as to the vapor phase, we multiply both sides of Eqs. (B10) and (B11) by 1 and $\mathbf{c}_i^*$, and then sum over all discrete velocities. After several algebraic manipulations, we obtain two continuity-like equations in the order of Kn and Kn^2,

$$\frac{\partial_1 s}{\partial t^*} + \frac{\partial_1}{\partial \mathbf{X}^*}\cdot(\mathrm{Da}\rho^*\mathbf{U}_v^*) = -\mathrm{Da}M^{*(1)}, \tag{B22}$$

$$\frac{\partial_2 s}{\partial t^*} = 0, \tag{B23}$$

while the corresponding momentum-like equations are

$$\frac{\partial_1(\mathrm{Da}\rho^*\mathbf{U}_v^*)}{\partial t^*} + \frac{\partial_1\left[\varepsilon(1-s)\rho^* P_v^{v*}\right]}{\partial \mathbf{X}^*} = \mathbf{G}^{*(1)}, \tag{B24}$$

$$\frac{\partial_2(\mathrm{Da}\rho^*\mathbf{U}_v^*)}{\partial t^*} = \left(\tau_g - \frac{1}{2}\right)\Delta t^*(c_s^*)^2\left\{\frac{\partial_1^2}{\partial \mathbf{X}^{*2}}(\mathrm{Da}\rho^*\mathbf{U}_v^*) + \frac{\partial_1}{\partial t^*}\frac{\partial_1}{\partial \mathbf{X}^*}\left[\frac{\varepsilon(1-s)\rho^* P_v^{v*} - 2(c_s^*)^2 s}{(c_s^*)^2}\right]\right\}. \tag{B25}$$

Again, we combine Eq. (B22) with Eq. (B23), and Eq. (B24) with Eq. (B25). The steady REV-scale governing equations for the vapor phase in porous media are obtained,

$$\frac{\partial}{\partial \mathbf{X}^*}\cdot(\rho^*\mathbf{U}_v^*) = -M^*, \tag{B26}$$

$$\mathbf{U}_v^* = -\frac{\varepsilon(1-s)}{\rho^*\mu^*\beta}\frac{\partial\left(\rho^* P_v^{v*}\right)}{\partial \mathbf{X}^*} + \frac{\mathrm{Da}}{\rho^*\mu^*\beta}\left(\tau_g - \frac{1}{2}\right)(c_s^*)^2\Delta t^*\frac{\partial^2}{\partial \mathbf{X}^{*2}}(\rho^*\mathbf{U}_v^*), \tag{B27}$$

where $\tau_g = \mu^*/[(c_s^*)^2\Delta t^*] + 0.5$. In conclusion, we demonstrate in this Appendix that the LB algorithm proposed in Sec. III can recover the separate-phase model for liquid-vapor two-phase flows in porous media at the REV scale.

APPENDIX C: DIMENSIONAL ANALYSIS OF LIQUID-VAPOR TWO-PHASE FLOWS IN POROUS MEDIA

We present the dimensional analysis for the separate-phase model, Eqs. (1)–(4), in this Appendix. We first define L as the characteristic length of porous media while introducing δ_l, δ_v, and δ_s to characterize the thicknesses of the corresponding liquid viscous boundary layer, vapor viscous boundary layer, and two-phase layer, respectively. For convenience, we also assume the interfacial mass transfer in porous media $M = 0$ in our following discussion.

For the liquid phase in Sec. IV B, we rewrite its continuity and momentum equations (1) and (2) in the two dimensions. We perform a dimensional analysis for these equations using the characteristic velocities U_l^0 (X direction) and V_l^0

(Y direction), characteristic liquid pressure $P_l^{l,0} = L\mu_l U_l^0/K$, and characteristic saturation s_0. In particular, we set s_0 less than but close to $s_b = 1$, as the two-phase flow in Sec. IV B is liquid dominant. In addition, we assign L and δ_l as the characteristic lengths in the X and Y directions, respectively. As a result, we obtain

$$\begin{gathered}\frac{\partial U_l}{\partial X} + \frac{\partial V_l}{\partial Y} = 0, \\ 1 \qquad \frac{\delta_l}{L}\frac{V_l^0}{U_l^0}\end{gathered} \tag{C1}$$

$$\begin{gathered}\frac{\varepsilon s \mu_l}{K_l} U_l = -\varepsilon s \frac{\partial P_l^l}{\partial X} + \mu_l \left(\frac{\partial^2 U_l}{\partial X^2} + \frac{\partial^2 U_l}{\partial Y^2} \right), \\ 1 \qquad s_0^3 \qquad \frac{\mathrm{Da}}{\varepsilon} s_0^2 \left(1 \qquad \frac{L^2}{\delta_l^2} \right)\end{gathered} \tag{C2}$$

and

$$\begin{gathered}\frac{\varepsilon s \mu_l}{K_l} V_l = -\varepsilon s \frac{\partial P_l^l}{\partial Y} + \mu_l \left(\frac{\partial^2 V_l}{\partial X^2} + \frac{\partial^2 V_l}{\partial Y^2} \right), \\ 1 \qquad \frac{L U_l^0}{\delta_l V_l^0} s_0^3 \quad \frac{\mathrm{Da}}{\varepsilon} s_0^2 \left(1 \qquad \frac{L^2}{\delta_l^2} \right).\end{gathered} \tag{C3}$$

Note that the terms listed beneath every equation represent the order of magnitude of each term in the equation. The scaling of Eqs. (C1)–(C3) reveals that in the liquid viscous boundary layer

$$V_l^0 \sim O\left(\frac{\delta_l}{L} U_l^0 \right), \quad \delta_l \sim O\left(\sqrt{\frac{\mathrm{Da}}{\varepsilon}} L s_0 \right) \text{ and } \frac{\partial P_l^l}{\partial Y} = 0. \tag{C4}$$

In a similar manner, we repeat the above procedure for Eqs. (3) and (4) for the vapor phase, in which we change the characteristic velocities as U_v^0 and V_v^0, the characteristic pressure $P_v^{v,0} = L\mu_v U_v^0/K$, and the characteristic length in the Y direction δ_v. In the vapor viscous boundary layer, the following relations are derived:

$$V_v^0 \sim O\left(\frac{\delta_v}{L} U_v^0 \right), \quad \delta_v \sim O\left[\sqrt{\frac{\mathrm{Da}}{\varepsilon}} L (1 - s_0) \right]. \tag{C5}$$

It should be pointed out that we obtained $\partial P_v^v/\partial Y = 0$ in the vapor viscous flow provided the limit $L \gg \delta_v$ holds. As for $\partial P_v^v/\partial X$, it is on the order of $(1 - s_0)^3$ in comparison to the X components of the viscous force and Darcy force. It is therefore rather trivial in the liquid-dominant flow. All these analyses imply the vapor pressure under this circumstance is insignificant in the vapor flow.

Next, we focus on estimating δ_s which characterizes the thickness of the two-phase layer. We derive the governing equation of s by taking the divergence on both sides of Eqs. (2) and (4), and then subtracting the resulting equations. With the aid of the continuity equations (1) and (3), we obtain

$$\begin{aligned}&\frac{3}{K}\left[\frac{\mu_l}{s^4}\mathbf{U}_l + \frac{\mu_v}{(1-s)^4}\mathbf{U}_v \right] \cdot \frac{\partial s}{\partial \mathbf{X}} \\ &\quad = -\sqrt{\frac{\varepsilon}{K}}\sigma J_c + \frac{1}{\varepsilon}\left[\frac{\mu_l}{s^2}\frac{\partial^2 \mathbf{U}_l}{\partial \mathbf{X}^2} + \frac{\mu_l}{(1-s)^2}\frac{\partial^2 \mathbf{U}_v}{\partial \mathbf{X}^2} \right] \cdot \frac{\partial s}{\partial \mathbf{X}},\end{aligned} \tag{C6}$$

where

$$J_c = \frac{dJ}{ds}\frac{\partial^2 s}{\partial \mathbf{X}^2} + \frac{d^2 J}{ds^2}\frac{\partial s}{\partial \mathbf{X}} \cdot \frac{\partial s}{\partial \mathbf{X}}. \tag{C7}$$

The function $J(s)$ is given by Eq. (8). Again, for a two-dimensional problem, Eq. (C6) is rewritten with the order of magnitude of each term as

$$\begin{gathered}\frac{3\mu_l}{K s^4}\left(U_l \frac{\partial s}{\partial X} + V_l \frac{\partial s}{\partial Y} \right) + \frac{3\mu_v}{K(1-s)^4}\left(U_v \frac{\partial s}{\partial X} + V_v \frac{\partial s}{\partial Y} \right) = F_c + F_l^\mu + F_v^\mu, \\ 1 \qquad \frac{\delta_l}{\delta_s} \qquad\qquad \gamma \qquad \gamma \cdot \frac{\delta_v}{\delta_s}\end{gathered} \tag{C8}$$

where

$$\begin{gathered}F_c = -\sqrt{\frac{\varepsilon}{K}}\sigma \left\{ \frac{dJ}{ds}\left(\frac{\partial^2 s}{\partial X^2} + \frac{\partial^2 s}{\partial Y^2} \right) + \frac{d^2 J}{ds^2}\left[\left(\frac{\partial s}{\partial X} \right)^2 + \left(\frac{\partial s}{\partial Y} \right)^2 \right] \right\}, \\ \frac{\sqrt{\varepsilon \mathrm{Da}}}{\mathrm{Ca}} s_0^6 \left(1 \qquad \frac{L^2}{\delta_s^2} \qquad 1 \qquad \frac{L^2}{\delta_s^2} \right)\end{gathered} \tag{C9}$$

$$\begin{gathered}F_l^\mu = \frac{\mu_l}{\varepsilon s^2}\left[\left(\frac{\partial^2 U_l}{\partial X^2} + \frac{\partial^2 U_l}{\partial Y^2} \right)\frac{\partial s}{\partial X} + \left(\frac{\partial^2 V_l}{\partial X^2} + \frac{\partial^2 V_l}{\partial Y^2} \right)\frac{\partial s}{\partial Y} \right], \\ \frac{\mathrm{Da}}{\varepsilon} s_0^2 \left(1 \qquad \frac{L^2}{\delta_l^2} \qquad \frac{\delta_l}{\delta_s} \qquad \frac{L^2}{\delta_l \delta_s} \right)\end{gathered} \tag{C10}$$

and

$$F_v^{\mu} = \frac{\mu_v}{\varepsilon(1-s)^2}\left[\left(\frac{\partial^2 U_v}{\partial X^2}+\frac{\partial^2 U_v}{\partial Y^2}\right)\frac{\partial s}{\partial X}+\left(\frac{\partial^2 V_v}{\partial X^2}+\frac{\partial^2 V_v}{\partial Y^2}\right)\frac{\partial s}{\partial Y}\right], \\ \frac{\mathrm{Da}}{\varepsilon}\gamma(1-s_0)^2\left(1 \qquad \frac{L^2}{\delta_v^2} \qquad \frac{\delta_v}{\delta_s} \qquad \frac{L^2}{\delta_v\delta_s}\right). \tag{C11}$$

In Eqs. (C8) and (C11), $\gamma = \mu^* U_0^* s_0^4/(1-s_0)^4$, with $\mu^* = \mu_v/\mu_l$ and $U_0^* = U_0^v/U_0^l$. We point out that in the two-phase layer in porous media, the flows of both the vapor and liquid phases are equally important, and both should be subject to the Darcy forces as well as pressure gradients. This insight leads to

$$\mu_v U_0^v \sim O\left(\frac{(1-s_0)^4}{s_0^4}\mu_l U_0^l\right), \quad \delta_s \sim O\left(\frac{\sqrt[4]{\varepsilon \mathrm{Da}}}{\sqrt{\mathrm{Ca}}}L s_0^3\right). \tag{C12}$$

As to the viscous forces in the two-phase layer, they are only considered when δ_l or δ_v is comparable to δ_s. For the flow discussed in Sec. IV B, we see $\delta_s \sim \delta_l$ and $\delta_s \gg \delta_v$. Therefore, the liquid flow in the two-phase layer is viscous in that problem, whereas the vapor viscosity only has significant effects within a thin region at the bottom of the two-phase layer.

APPENDIX D: STABILITY ANALYSIS ON THE DOUBLE-DISTRIBUTION FUNCTION LATTICE BOLTZMANN ALGORITHM

We perform the von Neumann linearized stability analysis on the double-distribution function LB algorithm developed in Sec. III. We chose the saturated liquid moving at a constant velocity far from any solid boundary as the reference, in which $s^0 = 1.0$, $P_l^{l*} = P^0$, and $\mathbf{U}_l^* = (U^0, 0)$. Note that we set $\mathbf{U}_l^*$ parallel to $\mathbf{c}_1^*(c^*, 0)$ as this would lead to the most unstable condition [43]. We decompose the distribution functions into two parts,

$$f_i^* = f_i^{0*} + f_i'^*, \tag{D1}$$

$$g_i^* = g_i^{0*} + g_i'^*, \tag{D2}$$

where f_i^{0*} and g_i^{0*} are the equilibrium distributions specified by Eqs. (20) and (21), but they use the reference fluid properties. For the local equilibria, f_i^{eq*} and g_i^{eq*}, and the source terms, F_i^* and G_i^*, we expand them into the Taylor series around the reference state. By neglecting all expanded terms at and beyond second order, we substitute the resulting expansions into the evolution equations (18) and (19), and obtain

$$\mathbf{f}'^*(t^*+\Delta t^*, \mathbf{X}^*+\mathbf{c}_i^*\Delta t^*) = \left[\left(1-\frac{1}{\tau_f}\right)\mathbf{I}+\mathbf{A}\right]\times \mathbf{f}'^*(t^*,\mathbf{X}^*)+\mathbf{B}\times \mathbf{g}'^*(t^*,\mathbf{X}^*), \tag{D3}$$

and

$$\mathbf{g}'^*(t^*+\Delta t^*, \mathbf{X}^*+\mathbf{c}_i^*\Delta t^*) = \left[\left(1-\frac{1}{\tau_g}\right)\mathbf{I}+\mathbf{C}\right]\times \mathbf{g}'^*(t^*,\mathbf{X}^*). \tag{D4}$$

In Eqs. (D3) and (D4), all variables are written in the matrix form for convenience. $\mathbf{f}'^* = \{f_0'^*, f_1'^*, f_2'^*, \ldots, f_8'^*\}^T$, $\mathbf{g}'^* = \{g'_0{}^*, g'_1{}^*, g'_2{}^*, \ldots, g'_8{}^*\}^T$, and $\mathbf{I}$ is the 9×9 identity matrix. The coefficient matrices, $\mathbf{A}$, $\mathbf{B}$, and $\mathbf{C}$, are independent of time and space and their components are

$$\mathrm{A}_{ij} = \frac{w_i}{\tau_f}\left[1+\frac{\mathbf{c}_i^*\cdot\mathbf{c}_j^*}{(c_s^*)^2}-\frac{\varepsilon\tau_f\Delta t^*}{\mathrm{Da}+\Delta t^*\varepsilon/2}\frac{\mathbf{c}_i^*\cdot\mathbf{c}_j^*}{(c_s^*)^2}\right], \tag{D5}$$

and

$$\mathrm{B}_{ij} = w_i\frac{2\varepsilon\mathrm{Da}\Delta t^*}{\mathrm{Da}+\Delta t^*\varepsilon/2}\frac{c_{ix}^* U^0}{(c_s^*)^2}, \tag{D6}$$

$$C_{ij} = \frac{H_i}{\tau_g}-\frac{w_i\rho^*\varepsilon P^0}{\tau_g(c_s^*)^2}+w_i\left(\frac{1}{\tau_g}-2\right)\frac{\mathbf{c}_i^*\cdot\mathbf{c}_j^*}{(c_s^*)^2}, \tag{D7}$$

with

$$H_i = \begin{cases} 1+\rho^*\varepsilon P^0/(c_s^*)^2, & i=0 \\ 0, & i\neq 0 \end{cases}. \tag{D8}$$

In Eqs. (D5)–(D8), $i = 0, 1, \ldots, 8$ and $j = 0, 1, \ldots, 8$. We then transform Eqs. (D3) and (D4) into the wave-number space through use of the Fourier transformation. After several mathematical manipulations, we obtain

$$\tilde{\mathbf{f}}'^*(t^*+\Delta t^*,\mathbf{k}) = \tilde{\mathbf{A}}\times\tilde{\mathbf{f}}'^*(t^*,\mathbf{k})+\tilde{\mathbf{B}}\times\tilde{\mathbf{g}}'^*(t^*,\mathbf{k}), \tag{D9}$$

$$\tilde{\mathbf{g}}'^*(t^*+\Delta t^*,\mathbf{k}) = \tilde{\mathbf{C}}\times\tilde{\mathbf{g}}'^*(t^*,\mathbf{k}), \tag{D10}$$

where $\tilde{\mathbf{A}} = \mathbf{D}\times[(1-1/\tau_f)\mathbf{I}+\mathbf{A}]$, $\tilde{\mathbf{B}} = \mathbf{D}\times\mathbf{B}$, and $\tilde{\mathbf{C}} = \mathbf{D}\times\mathbf{C}$, with the matrix $\mathbf{D} = \exp(-2\pi i\mathbf{k}\cdot\mathbf{c}_j^*\Delta t^*)\mathbf{I}$. The two wave-number-dependent perturbation functions are

$$\tilde{\mathbf{f}}'^*(t^*,\mathbf{k}) = \int \mathbf{f}'^*(t^*,\mathbf{X}^*)\exp(-2\pi i\mathbf{k}\cdot\mathbf{X}^*)d\mathbf{X}^*, \tag{D11}$$

and

$$\tilde{\mathbf{g}}'^*(t^*,\mathbf{k}) = \int \mathbf{g}'^*(t^*,\mathbf{X}^*)\exp(-2\pi i\mathbf{k}\cdot\mathbf{X}^*)d\mathbf{X}^*. \tag{D12}$$

As shown in Eqs. (D9) and (D10), stability will be achieved when the perturbations of the two distribution functions decay with time in the wave-number space. In the other words,

this is equivalent to say that the moduli of all eigenvalues of $\tilde{\mathbf{A}}$, $\tilde{\mathbf{B}}$, and $\tilde{\mathbf{C}}$ should be smaller than unity. For the simple homogenous flows where the wave number $\mathbf{k} = \mathbf{0}$, we computed that the eigenvalues of $\tilde{\mathbf{A}}$ are $1 - 1/\tau_f$, 1, and $(2\mathrm{Da} - \varepsilon\Delta t^*)/(2\mathrm{Da} + \varepsilon\Delta t^*)$ with the six, one, and two multiplicities, respectively, while those of $\tilde{\mathbf{B}}$ are all zeros. As to $\tilde{\mathbf{C}}$, its eigenvalues are $1 - 1/\tau_g$, -1, and 1 with the six, two, and one multiplicities. Therefore, for this simple problem ($\mathbf{k} = 0$), the stability conditions of the LB algorithm are $\tau_f > 1/2$ and $\tau_g > 1/2$. These are quite similar to those of the conventional D2Q9 LB model [43].

For general flows when $\mathbf{k} \neq \mathbf{0}$, the stability analysis of the LB algorithm becomes difficult as the stability will depend on multiple factors, including porous-medium properties (ε and Da), numerical setting (ΔX^*, τ_f and τ_g), flow conditions ($\mathbf{U}^0$, P^0), and fluid properties (μ^* and ρ^*). To specify complete and definite stability boundaries for general flows thus becomes notoriously challenging, and the results would also vary case by case. In this article, we restrict our discussion to the liquid-vapor two-phase flows in porous media in Sec. IV B. We computed the eigenvalues of $\tilde{\mathbf{A}}$, $\tilde{\mathbf{B}}$, and $\tilde{\mathbf{C}}$ and selected their maximum eigenvalue moduli, $|\lambda|_{\max}$, as the stability indicator. Through studying its dependence on Da, τ_f, and τ_g, we figured out the stability features of the LB algorithm for liquid-vapor two-phase flows. Interested readers can refer to Sec. IV B for more details.

[1] T. F. Russell, Rev. Geophys. **33**, 1035 (1995).
[2] H. Class and R. Helmig, Adv. Water Resour. **25**, 551 (2002).
[3] M. Sakai, N. Toride, and J. Šimůnek, Soil Sci. Soc. Am. J. **73**, 707 (2009).
[4] B. R. Scanlon and P. C. D. Milly, Water Resour. Res. **30**, 721 (1994).
[5] F. Tariku, K. Kumaran, and P. Fazio, Int. J. Heat Mass Transf. **53**, 3035 (2010).
[6] K. S. Udell, Int. J. Heat Mass Transf. **28**, 485 (1985).
[7] S. Mori and K. Okuyama, Int. J. Multiph. Flow **35**, 946 (2009).
[8] T. Defraeye, Appl. Energy **131**, 323 (2014).
[9] M. Zhang, H. Jiang, and R. Lim, Dry. Technol. **28**, 1307 (2010).
[10] K. Lange, P. Sui, and N. Djilali, J. Power Sources **196**, 3195 (2011).
[11] A. Xu, W. Shyy, and T. Zhao, Acta Mech. Sin. **33**, 555 (2017).
[12] P. Meakin and A. M. Tartakovsky, Rev. Geophys. **47**, RG3002 (2009).
[13] L. Chen, Q. Kang, B. A. Robinson, Y.-L. He, and W.-Q. Tao, Phys. Rev. E **87**, 043306 (2013).
[14] R. Alraoush, K. Thompson, and C. S. Willson, Soil Sci. Soc. Am. J. **67**, 1687 (2003).
[15] S. Whitaker, Transp. Porous Media **1**, 105 (1986).
[16] M. A. Hanlon and H. B. Ma, J. Heat Transf. **125**, 644 (2003).
[17] P. Yu, Y. Zeng, T. S. Lee, X. Chen, and H. T. Low, Int. J. Heat Fluid Flow **36**, 142 (2012).
[18] W. Liu, S. Peng, and K. Mizukami, Heat Mass Transf. **31**, 49 (1995).
[19] A. E. Scheidegger, *The Physics of Flow through Porous Media* (University of Toronto Press, Toronto, 1958).
[20] Z. Zeng and R. Grigg, Transp. Porous Media **63**, 57 (2006).
[21] G. Neale and W. Nader, Can. J. Chem. Eng. **52**, 475 (1974).
[22] A. Pantokratoras and E. Magyari, Transp. Porous Media **85**, 143 (2010).
[23] A. Nakayama, H. Koyama, and F. Kuwahara, Heat Mass Transf. **23**, 291 (1988).
[24] G. Lauriat and V. Prasad, J. Heat Transf. **109**, 688 (1987).
[25] P. Forchheimer, Wasserbewegung durch boden, Z. Ver. Dtsch. Ing. **45**, 1782 (1901).
[26] H. C. Brinkman, Appl. Sci. Res. **1**, 27 (1947).
[27] K. Vafai and C. L. Tien, Int. J. Heat Mass Transf. **24**, 195 (1981).
[28] N. Kladias and V. Prasad, J. Thermophys. Heat Transf. **5**, 560 (1991).
[29] Z. Chen, G. Huan, and B. Li, Transp. Porous Media **54**, 361 (2004).
[30] H. Belhaj, S. Mustafiz, F. Ma, and M. R. Islam, A new two phase extension of modified Brinkman formulation for fluid flow through porous media, in *Proceedings of 2005 ASME International Mechanical Engineering Congress and Exposition, Orlando, FL, 2005* (ASME, New York, 2005).
[31] S. Crone, C. Bergins, and K. Strauss, Transp. Porous Media **49**, 291 (2002).
[32] M. Chiang and H. Chu, J. Power Sources **160**, 340 (2006).
[33] K. Yuki, J. Abei, H. Hashizume, and S. Toda, J. Heat Transf. **130**, 012602 (2008).
[34] C. Wang and C. Beckermann, Int. J. Heat Mass Transf. **36**, 2747 (1993).
[35] C. Wang and C. Beckermann, Int. J. Heat Mass Transf. **36**, 2759 (1993).
[36] Z. Shi and X. Wang, Comparison of Darcy's law, the Brinkman equation, the modified N-S equation and the pure diffusion equation in PEM fuel cell modeling, in *Proceedings of the COMSOL Conference, Boston, 2007* (COMSOL Inc., Burlington, 2007).
[37] X. Shan and H. Chen, Phys. Rev. E **47**, 1815 (1993).
[38] Y. Shi, T. Zhao, and Z. Guo, Phys. Rev. E **70**, 066310 (2004).
[39] Y. Shi and J. E. Sader, Phys. Rev. E **81**, 036706 (2010).
[40] H. Kang, Y. Shi, and Y. Yan, Comput. Fluids **167**, 196 (2018).
[41] S. Chen, H. Chen, D. Martnez, and W. Matthaeus, Phys. Rev. Lett. **67**, 3776 (1991).
[42] S. P. Dawson, S. Chen, and G. D. Doolen, J. Chem. Phys. **98**, 1514 (1993).
[43] J. D. Sterling and S. Chen, J. Comput. Phys. **123**, 196 (1996).
[44] Z. Guo and T. Zhao, Phys. Rev. E **67**, 066709 (2003).
[45] X. He, S. Chen, and G. D. Doolen, J. Comput. Phys. **146**, 282 (1998).
[46] A. L. Kupershtokh and D. A. Medvedev, J. Electrost. **64**, 581 (2006).
[47] M. A. A. Spaid and F. R. Phelan, Jr., Phys. Fluids **9**, 2468 (1997).
[48] B. Manz, L. F. Gladden, and P. B. Warren, AIChE J. **45**, 1845 (1999).
[49] Q. Kang, P. C. Lichtner, and D. Zhang, J. Geophys. Res. **111**, B05203 (2006).
[50] G. Tang, W. Tao, and Y. He, J. Appl. Phys. **97**, 104918 (2005).
[51] Z. Chai, B. Shi, J. Lu, and Z. Guo, Comput. Fluids **39**, 2069 (2010).

[52] M. Liu, Y. Shi, J. Yan, and Y. Yan, Appl. Therm. Eng. **115**, 1348 (2017).
[53] Z. Guo and T. Zhao, Phys. Rev. E **66**, 036304 (2002).
[54] Z. Guo and T. Zhao, Numer. Heat Transf. B-Fundam. **47**, 157 (2005).
[55] S. Chen and G. D. Doolen, Annu. Rev. Fluid Mech. **30**, 329 (1998).
[56] C. Pan, M. Hilpert, and C. T. Miller, Water Resour. Res. **40**, W01501 (2004).
[57] I. Ginzburg and D. D'Humières, Phys. Rev. E **68**, 066614 (2003).
[58] L. Talon, D. Bauer, N. Gland, S. Youssef, H. Auradou, and I. Ginzburg, Water Resour. Res. **48**, W04526 (2012).
[59] G. Silva, L. Talon, and I. Ginzburg, J. Comput. Phys. **335**, 50 (2017).
[60] I. Ginzburg, Phys. Rev. E **77**, 066704 (2008).
[61] I. Ginzburg, G. Silva, and L. Talon, Phys. Rev. E **91**, 023307 (2015).
[62] I. Ginzburg, F. Verhaeghe, and D. d'Humières, Commun. Comput. Phys. **3**, 427 (2008).
[63] L. Hao and P. Cheng, Int. J. Heat Mass Transf. **53**, 1908 (2010).
[64] J. Yang and E. S. Boek, Comput. Math. Appl. **65**, 882 (2013).
[65] O. Dardis and J. McCloskey, Phys. Rev. E **57**, 4834 (1998).
[66] S. D. C. Walsh, H. Burwinkle, and M. O. Saar, Comput. Geosci. **35**, 1186 (2009).
[67] G. G. Pereira, B. Wu, and S. Ahmed, Phys. Rev. E **96**, 063108 (2017).
[68] Z. Guo, C. Zheng, and B. Shi, Phys. Rev. E **65**, 046308 (2002).
[69] Y. Qian, D. D'Humières, and P. Lallemand, Europhys. Lett. **17**, 479 (1992).
[70] S. Chen, Z. Wang, X. Shan, and G. D. Doolen, J. Stat. Phys. **68**, 379 (1992).
[71] Z. Guo, C. Zheng, and B. Shi, Chin. Phys. **11**, 366 (2002).
[72] P. Lallemand and L. Luo, Phys. Rev. E **61**, 6546 (2000).
[73] D. A. Wolf-Gladrow, *Lattice-gas Cellular Automata and Lattice Boltzmann Models: An Introduction* (Springer, Berlin, 2004).
[74] S. Whitaker, *The Method of Volume Averaging* (Academic Publishers, Amsterdam, 1999).